Theoretical Studies of Nano Self-Assembly

by

Peter Alexander Greaney

M.Eng. (University of Oxford) 1998

A dissertation submitted in partial satisfaction of the
requirements for the degree of
Doctor of Philosophy

in

Engineering–Materials Science and Mineral Engineering

in the

GRADUATE DIVISION
of the
UNIVERSITY of CALIFORNIA at BERKELEY

Committee in charge:

Professor Daryl C. Chrzan, Chair
Professor Eugene E. Haller
Professor Panayiotis Papadopoulos

Fall 2003

The dissertation of Peter Alexander Greaney is approved:

Chair Date

Date

Date

University of California at Berkeley

Fall 2003

Theoretical Studies of Nano Self-Assembly

Peter Alexander Greaney

Abstract

Theoretical Studies of Nano Self-Assembly

by

Peter Alexander Greaney

Doctor of Philosophy in Engineering–Materials Science and Mineral Engineering

University of California at Berkeley

Professor Daryl C. Chrzan, Chair

The role of surface strain in the growth of self-assembling nanostructures is investigated theoretically. The magnitude of the strain at the surface of a film generated by a buried array of misfit dislocations is calculated. It is demonstrated that such a film provides a suitable substrate for wavelength controlled spinodal decomposition of a second film grown on top of it. The role of homogeneous substrate strain is discussed in the context of how it affects diffusion processes and how these, in turn, impact island growth. An existing mean-field analysis of island growth is extended to include anisotropic diffusion. The results of the mean field calculations are compared with kinetic Monte Carlo simulations. It is found that anisotropy in adatom hopping reduces the density of stable islands. It is also found that although the shape of island size distribution is sensitive to island relaxation processes, it is not discernibly affected by hopping anisotropy with ratios $\frac{D_{xx}}{D_{yy}}$ up to 16. A diffusion mechanism involving the recently discovered surface crowdion is hypothesised and the implications of this mechanism on island growth are studied through KMC simulations.

Professor Daryl C. Chrzan
Dissertation Committee Chair

To my parents.

Contents

Chapter 1

Introduction

Much of the behaviour of materials at the nanometre length scale differs from the behaviour of bulk materials. For electrical properties this is because quantum effects become important at very small sizes and many of the assumptions upon which explanations of bulk properties depend (in particular wave properties) are no longer valid when dealing with countable numbers of atoms. The mechanical properties of a material also change when length scales become very small, however this is due to the reduction in population of mechanically important crystal defects (e.g. dislocation sources and grain boundaries), and because of the interaction between elastic strain fields and the physical boundaries and free surfaces of the material. Understanding the behaviour of materials on the nanometre length scale has, in recent years, become an important area of materials science due to both the technological promise of nano-structured materials, and the furthering of our fundamental understanding of materials.

Useful devices that exploit nanoscale materials properties usually require regular arrays of nanoscale structures. For example arrays of quantum dots (structures that have at least one bound state in the band gap due to confinement) can be used to make lasers and photodetectors of a desired wavelength. Arrays of magnetic materials are used for data recording. Films of nano-crystalline diamond are used for super-hard coatings. Creating arrays of small scale features with the desired degree of uniformity of feature size, shape, composition and even spacing is non-trivial, especially as these features may be too small to pattern by lithography. Processes in which desired materials structures grow spontaneously are a promising avenue for low cost fabrication of nano-structured materials. These so called "Self-organised assembly processes" offer large area patterning at the expense of the long

range (translational) order of the array of nano features. Spontaneously occurring regular structures are well known in materials science–a common example is the lammellar structure of a solidified eutectic alloy. A characteristic length scale of the heterogeneous structures arises through the competition between thermodynamic and kinetic driving forces each favouring different length scales. Hence understanding the thermodynamics and kinetics of crystal growth, morphological, and structural transitions at the nanoscale has also become an important area of materials research.

This thesis offers a theoretical exploration of two topics in "nanoscale self-assembly." In the first section the feasibility of using a strain template to control the wavelength of spinodal decomposition within a film is discussed. In the second section the effects of anisotropic surface diffusion and a newly identified surface transport mechanism on the early stages of island growth are investigated.

Chapter 2

Segregation in Strained Films

2.1 Introduction

There are many cases where it is desirable to create an array of small particles or nano-crystals with a narrow size distribution. One particular example is the case of longitudinal magnetic recording, where a film of single-domain ferromagnetic particles is used to digitally store information.

In computer hard-drives the substrate for the magnetic film is a glass or aluminium disc. The particles in the film have their soft direction of magnetisation oriented at random in the plane of the disc. Bits of data are written by magnetising a collection of the particles in a particular orientation in the film, with a local magnetic field. Approximately 100 particles are needed in each bit to give a large signal to noise ratio for reading back the data. Each bit does not have a predefined position but, rather, bits are written one after another along concentric circular tracks as the disc rotates. The width of a track is determined by the width of the read-write head and the servoing precision of the arm that holds it. The length of the bit is limited by how sharp the boundary can be written (and detected) between bits in the track. Improving areal bit densities requires writing smaller bits with sharper boundaries.

Writing sharp bit boundaries that do not blur over time requires the magnetic particles not to be susceptible to thermal randomisation of their magnetic moments and that particles not be interacting magnetically. Bits can be made smaller and their boundaries sharper by reducing the size of the magnetic particles. However, there is a size threshold below which the energy required to flip the particles' directions of magnetisation is attainable

by thermal fluctuations over reasonable time scales. Creating efficient recording media at this so called "superparamagnetic" limit requires all the magnetic particles to be larger than some critical size but as close to it as possible. There needs to be a monodisperse distribution of particle sizes with the whole distribution just larger than some critical size (approximately 8nm for the currently used non antiferromagnetically coupled Co alloy films [1]).

Arrays of islands and particles grown by standard physical deposition processes exhibit a size distribution as broad as the average particle size [2]. This is because there is only one characteristic length scale in the problem (the average island size). To create cost effective longitudinal recording media that are functional at the superparamagnetic limit requires finding a "self-assembly" process for growing a monodisperse film of magnetic nanoparticles. In this chapter the feasibility of creating an array of particles with a narrow size distribution by using the strain from an array of misfit dislocations to control the wavelength of a spinodal decomposition reaction is presented.

2.2 Background

2.2.1 Misfit dislocations

Misfit dislocations are observed at the film-substrate interface of lattice mismatched hetroepitaxial films when the strain energy of the film reaches some critical value (that is usually proportional to film thickness). In epitactic systems of small or moderate mismatch misfit dislocations are only energetically favourable in films thicker than some critical thickness. Since these dislocations are only stable at a finite film thickness, they must nucleate at the surface and glide to the film substrate interface. Thus, as the glide plane lies necessarily at an angle to the film substrate interface the Burgers vector contains a component out of the plane of the interface. As only the edge component of the Burgers vector projected onto the substrate interface is strain relaxing,[1] surface nucleated misfit dislocations give poor stress relief. Epitactic systems with large mismatches on the other hand can have critical film thicknesses of less than a monolayer. These films necessarily grow as three dimensional islands which relax misfit strain by directly incorporating pure edge dislocations

[1] Screw dislocations are pure shear and will not relax misfit strains.

at the island edges as they grow. This results in a regular network of misfit dislocations with a high degree of misfit relaxation [3, 4]. Woodall and coworkers have shown that by growing at low temperatures, the average separation of these pure edge misfit dislocations in a system with an 11% mismatch (InAs on GaP(001)) can be as close as 4.1 nm with only a 0.1 nm deviation in regularity of their position (leading to a 85% strain relaxation).

Misfit dislocations in thin films have associated with them a strain that is nonzero at the film surface. Traditionally, misfit dislocations have proved to be a problem in microelectronic devices as they ruin their optoelectronic properties. Consequently, much effort has been spent on trying to eliminate misfit dislocations. However, it has been shown both theoretically [5, 6, 7, 8] and experimentally [9] that the surface strain from a network of misfit dislocations can provide regions of preferential island nucleation during epitaxy. This makes it possible to employ a network of misfit dislocations in an epitaxial film as a patterned substrate for the growth of a self-assembled array of nano-crystals. The long range order for the array comes from the elastic interactions of the dislocations and the fine scale is controlled by the misfit strain.

2.2.2 Spinodal decomposition of films

The first thermodynamic description of spinodal decomposition in bulk binary alloys was given by Cahn and Hilliard in 1959 [10, 11, 12]. They proposed that the free energy density of binary alloys (in direct analogy with magnetic materials) depended on their local composition (magnetisation), the gradient of their local composition (exchange energy), and elastic strain resulting from volume changes associated with local concentration changes (magnetostriction and anisotropy energy). Mathematically this is can be described by

$$\langle f_{\text{tot}} \rangle = \frac{1}{V} \int_V dr^3 \left(f_{\text{ch}} \left(C(\boldsymbol{r}) \right) + \Gamma \left| \nabla C(\boldsymbol{r}) \right|^2 + \mathcal{F}_{\text{el}} \left\{ C(\boldsymbol{r}) \right\} \right), \tag{2.1}$$

where V is the volume of the solid, $\langle f_{\text{tot}} \rangle$ is the mean total free energy density, $f_{\text{ch}} \left(C(\boldsymbol{r}) \right)$ is the local chemical free energy density, $\mathcal{F}_{\text{el}} \left\{ C(\boldsymbol{r}) \right\}$ is the local elastic energy density which is a functional of the concentration distribution, $C(\boldsymbol{r})$, and Γ represents the contribution to the free energy density from the gradient in the local concentration. Cahn and Hilliard found that in bulk solids elastic strain can suppress the tendency for spinodal decomposition and thus reduce the critical temperature below which segregation occurs. The consequence of the gradient energy term, Γ, is that the infinitely long wavelength mode of segregation

is the first mode to become unstable as the gradient is minimised.

Observations of segregation in III-V semiconductor alloy films at temperatures above the critical temperature for segregation in the bulk led Glas to reexamine the elastic strains during spinodal decomposition in films [13]. Glas calculated the elastic energy of an epitaxial film with a sinusoidally modulated lattice parameter on a substrate where the direction of modulation is parallel to the substrate interface. He assumed that the film and substrate were continuous across the interface and that they were both elastically isotropic with the same elastic moduli (which was independent of concentration). Glas found the mean elastic energy density of the heterogeneity in the film (with the period of the heterogeneity of the same order as the film thickness) to be reduced relative to the mean strain energy density of a similar heterogeneity in an infinite solid by a factor of approximately 0.45.

In Glas' calculation it is assumed that the composition is uniform through the film thickness and only modulated parallel to the film surface. In a real system, however, one expects that the true surface modes of segregation will have the amplitude of segregation as a maximum at the surface and decay into to the film (indirect analog of the difference between Rayleigh waves and bulk sound waves). The form of such a soft surface mode has been found analytically by Ipatova and coworkers [14] for cubic materials. These workers express the elastic energy as a functional, $\mathcal{F}_{\rm el}\{C(\boldsymbol{r})\}$, of an arbitrary composition distribution using the elastic Green's function for a cubic half infinite solid. They then determine the form of $C(\boldsymbol{r})$ that minimises the total Helmholtz free energy of the system. They examined segregation modes that extend through the film thickness, modes that are localised at the film interface and modes that are localised at the free surfaces and found the intuitive result that modes localised at the surface have the lowest free energy. The composition amplitude of these surface modes decay exponentially into the bulk of the alloy over a characteristic distance on the order of the modulation period. Ipatova and coworkers find that in the limit that this attenuation length is much smaller than the film thickness (*i.e.*, a decomposing half infinite solid) the *elastic* energy from the surface mode is reduced relative to that of a bulk mode by a factor of $\frac{c_{11}}{2(c_{11}+c_{12})}$ with c_{11}, c_{12}, c_{44} the elastic moduli in Voigt notation. Their calculation neglects composition gradient contributions to the free energy.

2.2.3 Other spontaneous transformations in films

The stability of a planar surface in a tetragonally strained, homogeneous, half infinite solid has been investigated by Asaro and Tiller [15], and Srolovitz [16]. These researchers found that any film under a compressive misfit strain is unstable to the formation of long wavelength undulations.

Glas has considered theoretically the stability of homogeneous flat films and homogeneous half infinite solids under biaxial compressions to spontaneous transformations that involve both a morphological change and heterogeneity [17, 18]. He found that the energy of such a coupled transformation is lower than either a sole composition modulation or a sole surface undulation. In his analysis he neglects gradient energy and only considers homogeneous strains.

Jonsdottir and Freund have investigated theoretically the formation of undulations in the surfaces of films driven by the strain field from a buried network of misfit dislocations [19].

2.2.4 Extent of transformation

The stability analyses outlined above only determine weather a spontaneous transformation will occur. Intrinsic to these approaches are linear expansions of the thermodynamic properties in and around the homogeneous state. These linear approximations quickly break down as the amplitude of perturbations in the transformation's order parameter grow. So, although these stability treatments can predict the amplification rate of different modes of transformation in the early stages of the reaction they cannot predict final structures. There have been two sets of studies on the evolution of segregation in films.

Voorhees and *et al.* [20, 21, 22], and Ipatova and coworkers [23] have investigated the development of segregation during the growth of a film. Their model describes an observed *kinetic* segregation instability which can occur during film growth. In this model only atoms on the surface of a growing film are mobile. As atoms are continually added to the surface (from the deposition process) surface composition fluctuations are frozen into the growing film. The stability of the film to fluctuations in the concentration is dependent on the rate at which atoms are deposited on the surface.

Léonard and Desai have numerically tracked the evolution of heterogeneities in segregating films [24, 25, 26]. Central to this work is the assumption that the chemical

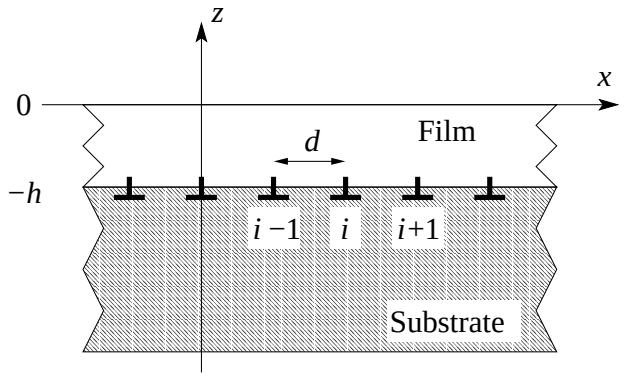

Figure 2.1: Diagram showing infinite one dimensional array of pure edge misfit dislocations. These are regularly spaced with a separation d at the interface of a film of thickness h. The Burgers vectors all lie in substrate interface.

free energy term in Eqn. 2.1 takes the form of a Ginzburg-Landau potential. Here the exact form of chemical free energy density is assumed to be *un*important, and the overall double-welled shape of the potential (which *is* deemed significant) is approximated with a polynomial. These researchers have also considered morphological instabilities in films coupled to ordering reactions [27],[2] and a *kinetic* instability in the presence of an array of misfit dislocations, where they find that segregation reduces the critical thickness for the introduction of dislocations.

2.3 Surface strain from a network of misfit dislocations

The first step in examining feasibility of using misfit dislocations to pattern a substrate is to determine the size of the strain contrast that can be produced. The strain tensor, $\boldsymbol{\varepsilon}^{\mathrm{MF}}(\boldsymbol{r})$ arising from a one dimensional array of pure edge misfit dislocations, arranged in the geometry shown in figure 2.1, can be calculated by summing the contributions from all the interfacial dislocations in the array. Mathematically this is

$$\boldsymbol{\varepsilon}^{\mathrm{MF}}(\boldsymbol{r}) = \boldsymbol{\varepsilon}^{\mathrm{L}}(\boldsymbol{r}) + \sum_{i=-\infty}^{\infty} \boldsymbol{\varepsilon}^{\mathrm{D}}(\boldsymbol{r} - id\hat{\boldsymbol{x}}; h), \tag{2.2}$$

[2]Ordering reactions are similar to spinodal reactions in that the system becomes continuously unstable (*i.e.*, not in a local equilibrium) to the growth of segregating modes. In ordering reactions the unstable modes of segregation are at the Brillouin zone edge while for spinodal decomposition the unstable modes are at the gamma point.

where $\boldsymbol{\varepsilon}^{\mathrm{L}}(\boldsymbol{r})$ is the unrelaxed strain tensor from the lattice mismatch (a step function), $\hat{\boldsymbol{x}}$ is the unit vector in the x direction, and $\boldsymbol{\varepsilon}^{\mathrm{D}}(\boldsymbol{r};h)$ is the strain distribution around an isolated misfit dislocation buried a distance h below the free surface. This last term can be calculated, following the procedure outlined in section 3.5 of Hirth and Lothe [28], as the sum of the strain from an isolated dislocation in a bulk (infinite) solid, an image dislocation, and a corrective strain field used to cancel tractions on the free surface. For the case of an edge misfit dislocation, defining the image such that both image and misfit dislocations have the same Burgers vector and line direction results that the only nonzero element of the surface strain comes from the corrective stress. This is given by

$$\varepsilon^{\mathrm{D}}_{xx}(\boldsymbol{r}_{z=0};h) = 2b\frac{hx^2}{\pi(h^2+x^2)^2}, \tag{2.3}$$

where $\boldsymbol{r}_{z=0}$ is the position vector of points on the free surface, and b is the magnitude of the Burgers vector. Note that this is independent of the Poisson ratio.

Summing Eqn. 2.3 over all the dislocations in two perpendicular sets of misfit dislocations gives strains at the free surface of

$$\varepsilon_{xx}(x,y,0) = \frac{b\left(2\tilde{h}+\sinh(2\tilde{h})-2\cos(\tilde{x})\left(\tilde{h}\cosh(\tilde{h})+\sinh(\tilde{h})\right)\right)}{2d\left(\cos(\tilde{x})-\cosh(\tilde{h})\right)^2}, \tag{2.4}$$

$$\varepsilon_{yy}(x,y,0) = \frac{b\left(2\tilde{h}+\sinh(2\tilde{h})-2\cos(\tilde{y})\left(\tilde{h}\cosh(\tilde{h})+\sinh(\tilde{h})\right)\right)}{2d\left(\cos(\tilde{y})-\cosh(\tilde{h})\right)^2}, \tag{2.5}$$

$$\varepsilon_{xy}(x,y,0) = 0, \tag{2.6}$$

where $\tilde{h} = h\frac{2\pi}{d}$, $\tilde{x} = x\frac{2\pi}{d}$, $\tilde{y} = y\frac{2\pi}{d}$, and d is the dislocation separation. It can be seen that as the film becomes thick in comparison to the dislocation spacing (*i.e.*, $h \ll d$) the strain becomes $\frac{b}{d}$ as expected. Figure 2.2 shows the surface strain topography from a network of dislocations that fully relax a misfits strain, that is, $\frac{b}{d} = \frac{|a_f - a_s|}{a_s}$ (where a_s and a_f are the lattice constants of the substrate and film respectively). From plot (d) in figure 2.2 it can be seen that the amplitude of the residual surface strains can be an appreciable fraction of the original misfit strain when the film thickness approaches that of the dislocation spacing. Hence one might expect that using a dislocated thin film as a substrate for the growth of a second film may provide a strong template for self organised growth. However, from plot (c) it can be seen that if the film becomes too thin then the dislocations produce a more complicated strain topography that could be considered as potential energy walls

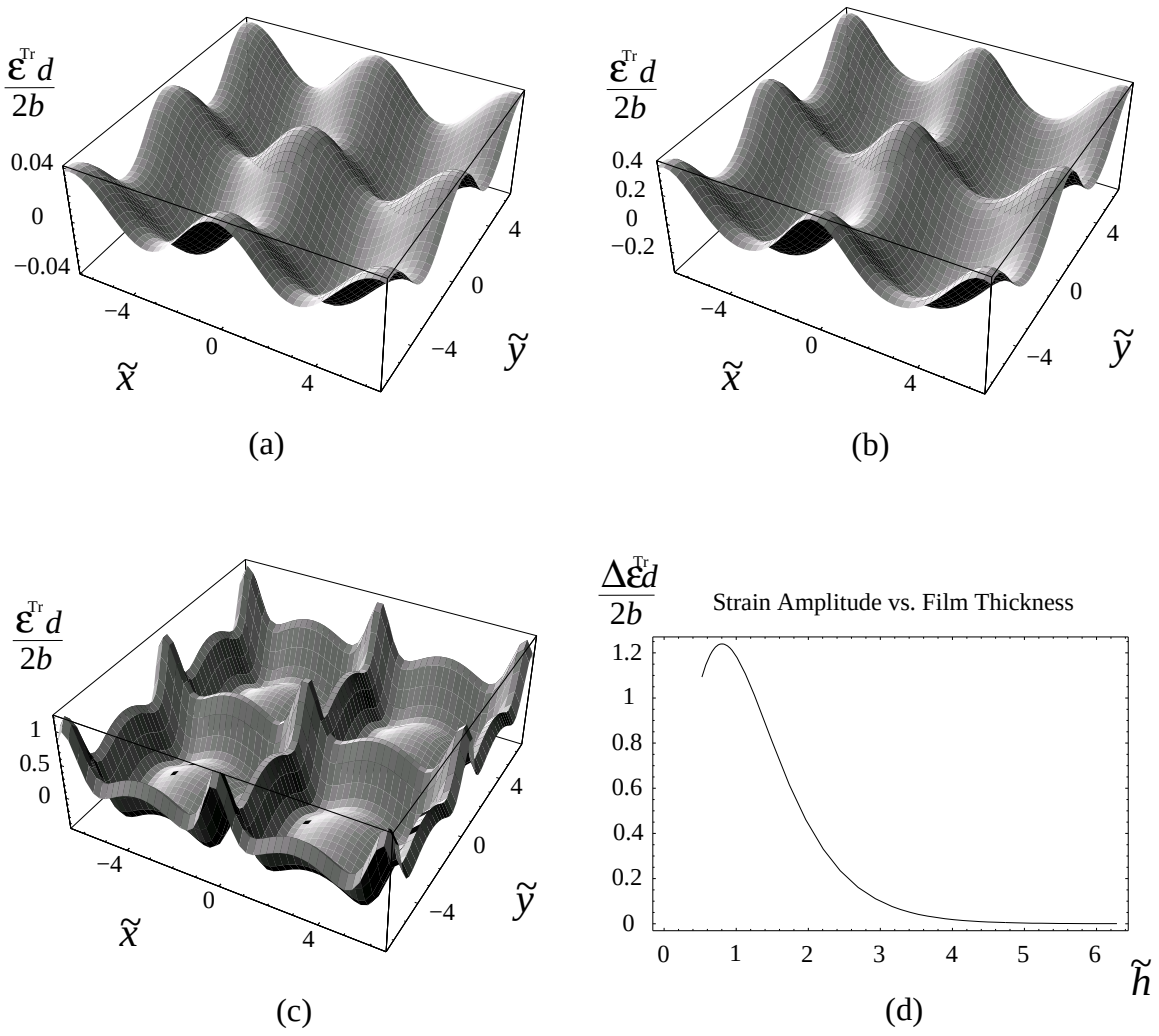

Figure 2.2: Variation in the trace of the surface strain tensor over a dislocated film. The trace is plotted as a fraction of the original misfit strain, $1 - \frac{\varepsilon^{Tr} d}{2b}$. It is assumed that the dislocations fully relax the lattice mismatch. Plot (a) is for a film thickness equal to the dislocation spacing, (b) for $h = \frac{d}{2}$, and (c) for $h = \frac{d}{5}$. Plot (d) shows the change in fractional strain amplitude $(\varepsilon^{Tr}(0,0,0) - \varepsilon^{Tr}(\pi,\pi,0))$ with $\tilde{h}$. Note that the decrease in strain amplitude at small film thicknesses is because the film thickness sets the decay length of the dislocation strain field, if this is too small the dislocations do not relax the film in between the dislocations. This can be seen in plot (c).

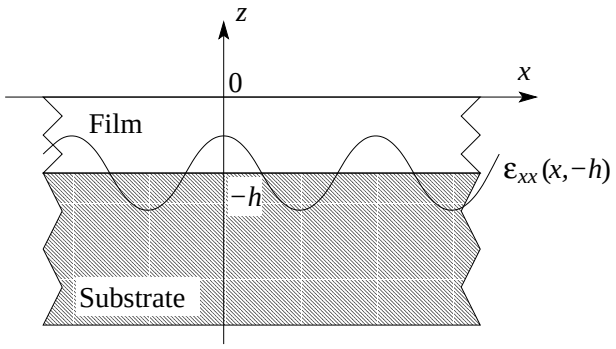

Figure 2.3: Diagram showing infinite homogeneous isotropic elastic film on a rigid substrate with a periodic lattice constant. The origin is at the free surface of the film.

or trenches. This is of particular relevance to the work of Kern and coworkers [9] who experimentally grow a self ordering array of Ag nanoclusters on a dislocated Ag(111) film only two monolayers thick (of course at these thicknesses the validity of elasticity theory also becomes suspect).

2.4 Stability of a film on a strain patterned substrate

2.4.1 Model

The stability of a homogeneous film deposited on top of the dislocated film discussed above is now considered. The rudimentary model of spinodal decomposition employed here is depicted in Fig. 2.3. An elastically isotropic binary A-B alloy is deposited on a rigid substrate (*i.e.*, it is assumed that the film is much more compliant than the substrate as might be the case for an FCC metal on a semiconductor substrate) with a periodically varying lattice parameter along the x-direction only. The pure metals A and B, and all their alloys, are assumed to have identical surface energies. The film is initially compositionally homogeneous, with a concentration C_o of B, such that there is no *net* lattice mismatch with the substrate. This results in a sinusoidal interfacial strain in the film of

$$\varepsilon_{xx}(x,-h) = \varepsilon_s \cos(\kappa_s x), \tag{2.7}$$

which can be considered a Fourier component of the misfit dislocation strain field given in equation 2.6. The elastic moduli of the film are assumed to be independent of composition, and the two species comprising the film (A and B) have different molar volumes (V_A and

V_B respectively). Any local change in concentration is accompanied by a change in the local equilibrium lattice parameter.

To analyse the stability of the homogeneous film with respect to segregation it is necessary to determine the change in the mean free energy density of the film (given in Eqn. 2.1) associated with the introduction of a concentration wave with infinitesimal amplitude. The analysis presented here follows closely that of Cahn [11], and is similar in spirit to the prior analyses of thin film spinodal decomposition [13, 14]. In performing the linear stability analysis, one must assume a form for the perturbation. Here the concentration is chosen to be

$$C(x, y, z) = C_o + \Delta C \cos(\kappa_c x), \tag{2.8}$$

with $\Delta C \ll C_o$. Note that the composition fluctuation is assumed to be uniform throughout the film thickness. It is not known *a priori* how the amplitude of the composition wave might change through the film thickness. Hence, the assumed structure of this perturbation may, in fact, *preclude* the most unstable mode. However, if the film is unstable with respect to the growth of this constrained composition fluctuation, then the film is certainly unstable to the growth of the lowest energy concentration fluctuation. Further, in the limit $h \ll \kappa_c^{-1}$, the assumed form is correct.

2.4.2 Chemical contributions to free energy

The chemical free energy density, in 2.1 is approximated to second order in ΔC by a Taylor series expansion about the initial concentration,

$$f_{\rm ch}(C) = f_0 + f_1 \Delta C \cos(\kappa_c x) + \frac{f_2 \Delta C^2 \cos^2(\kappa_c x)}{2!}, \tag{2.9}$$

with $f_i \equiv \left.\frac{\partial^i f}{\partial C^i}\right|_{C=C_o}$. Spinodal decomposition can occur only if the compositional free energy surface is concave down, *i.e.*, $f_2 < 0$.

The gradient term in Eqn. 2.1 can be derived by also expanding the local chemical free energy density in terms of the local gradient in the composition [29]. Symmetry dictates that the first nonzero term in this expansion contains $|\nabla C(\boldsymbol{r})|^2$. More intuitively one can see that Γ plays the role of an excess interfacial free energy. Averaging the local chemical and local gradient contributions to the free energy over the film volume and combining them in the *total* mean *chemical* contribution to the free energy density gives

$$\langle f_{\rm TC} \rangle = f_0 + \left(\frac{f_2}{4} + \frac{\Gamma \kappa_c^2}{2} \right) \Delta C^2. \tag{2.10}$$

2.4.3 Elastic contribution to free energy

To complete the computation of the free energy change associated with a composition fluctuation, one must compute the associated elastic energy, $\mathcal{F}\{C(\boldsymbol{r}\})$. This is a functional of the concentration distribution because the elastic strain around any local volume change drops off as $\sim r^{-3}$. Fixing the shape of the concentration profile enables the resulting elastic energy density distribution, $E_{\rm el}(x,z)$, to be calculated. The total strain tensor, $\boldsymbol{\varepsilon}^{\rm T}(x,z)$, has three components; $\boldsymbol{\varepsilon}^{\rm T}(x,z) = \boldsymbol{\varepsilon}^{\rm S}(x,z) + \boldsymbol{\varepsilon}^{\rm SF}(x,z) + \boldsymbol{\varepsilon}^{\rm C}(x,z)$. Here $\boldsymbol{\varepsilon}^{\rm S}(x,z)$ is the strain imposed by the film being epitaxial on a substrate with a varying lattice constant. This only depends on the amplitude, ε_s and wave number, κ_s, of the substrate strain imposed at the interface (Eqn. 2.7). The term $\boldsymbol{\varepsilon}^{\rm SF}(x,z)$ is the purely dilatational stress free strain that accompanies a local change in concentration. This is approximated to first order in the local concentration change as

$$\boldsymbol{\varepsilon}^{\rm SF}(x,z) \approx \frac{\Delta V \Delta C}{3} \cos(x\kappa_c), \tag{2.11}$$

where ΔV is the difference in the molar volumes of the two components, $V_B - V_A$. While the film changes volume locally it must remain continuous (*i.e.*, the total displacement vector must be continuous everywhere). This requirement produces an elastic strain field, $\boldsymbol{\varepsilon}^{\rm C}(x,z)$, such that $\boldsymbol{\varepsilon}^{\rm T}(x,z)$ satisfies the equations of compatibility everywhere. Both the stress free strain and the compatibility strain depend only on the amplitude, ΔC, and the wavenumber, κ_c, of the heterogeneity (Eqn. 2.8). Formally the elastic energy density is $\sum_{i,j=1}^{3} \frac{1}{2}\left(\varepsilon_{ij}^{\rm S} + \varepsilon_{ij}^{\rm C}\right)\sigma_{ij}$, so it is only necessary to determine the strain field imposed by the substrate and the compatibility strain to find the elastic energy. This problem may be solved by writing Hooke's law incorporating the stress free strain, and then solving the appropriate partial differential equation. This approach, while obviously correct, is not the most intuitive. Here, an alternative, more intuitive solution is presented.[3]

2.4.3.1 Strain imposed by substrate

The substrate imposes a condition of plane strain that is independent of the concentration fluctuation, so $\boldsymbol{\varepsilon}^{\rm S}(x,z)$ must independently satisfy the condition of compatibility, and thus can be found by solving the biharmonic equation,

$$\nabla^4 \psi = 0, \tag{2.12}$$

[3]It can be shown that the approach presented here yields a solution identical to that arising from the straightforward, but less intuitive, method.

where ψ is the Airy stress function. This equation is simply the plane strain compatibility condition

$$\frac{\partial^2 \varepsilon_{xx}}{\partial z^2} + \frac{\partial^2 \varepsilon_{zz}}{\partial x^2} - 2\frac{\partial^2 \varepsilon_{xz}}{\partial x \partial z} = 0, \tag{2.13}$$

where the strains are written in terms of the stresses (using Hooke's law). The stresses are in turn written in terms of the Airy stress function which satisfies the equilibrium equations,

$$\frac{\partial \sigma_{xx}}{\partial x} + \frac{\partial \sigma_{xz}}{\partial z} = 0, \tag{2.14}$$

$$\frac{\partial \sigma_{zz}}{\partial z} + \frac{\partial \sigma_{xz}}{\partial x} = 0, \tag{2.15}$$

by defining the stress function such that

$$\sigma_{xx} = \frac{\partial^2 \psi}{\partial z^2}, \tag{2.16}$$

$$\sigma_{zz} = \frac{\partial^2 \psi}{\partial x^2}, \tag{2.17}$$

$$\sigma_{xz} = -\frac{\partial^2 \psi}{\partial x \partial z}. \tag{2.18}$$

The general form of the stress function for the current problem is found by separation of variables to be

$$\psi(x,z) = \Big(A\sin(\kappa x) + \cos(\kappa x)\Big)\Big((\alpha_0 + \alpha_1 z)\sinh(\kappa z) + (\beta_0 + \beta_1 z)\cosh(\kappa z)\Big). \tag{2.19}$$

$\boldsymbol{\varepsilon}^{\mathrm{S}}(x,z)$ is computed by finding the integration constants ($A, \alpha_0, \alpha_1, \beta_0$ and β_1) that satisfy the boundary conditions of no surface tractions and coherence with the substrate.

2.4.3.2 Compatibility strain

The compatibility strain, $\boldsymbol{\varepsilon}^{\mathrm{C}}(x,z)$, is found by first considering the elastic strain tensor, $\boldsymbol{\varepsilon}^{\mathrm{B}}(x)$, of a bulk solid containing a concentration plane wave, and then adding a corrective strain to satisfy boundary conditions. The concentration plane wave in a bulk solid has been studied extensively by Cahn [11], who found the solid completely elastically relaxed in the direction of the concentration modulation and completely elastically constrained in all directions normal to it. This gives a stress state in the bulk solid of

$$\sigma^{\mathrm{B}}_{xy}(x) = \sigma^{\mathrm{B}}_{yz}(x) = \sigma^{\mathrm{B}}_{xz}(x) = 0, \tag{2.20}$$

$$\sigma^{\mathrm{B}}_{xx}(x) = 0, \tag{2.21}$$

$$\sigma^{\mathrm{B}}_{zz}(x) = \sigma^{\mathrm{B}}_{yy}(x) = -2\mu\varepsilon_c \frac{1+\nu}{1-\nu}\cos(\kappa_c x), \tag{2.22}$$

where $\varepsilon_c = \frac{\Delta V \Delta C}{3}$, and μ is the shear modulus.

This "bulk" like strain field can be transformed into the strain state for a *film* containing a concentration perturbation by the sequential application of two plain strain deformations. The first enforces the condition of equilibrium at the free surface by applying to it tractions $-\sigma^{\mathrm{B}}_{zz}(x,0)\hat{\boldsymbol{z}}$ whilst constraining the interface to not move. The second corrective deformation strains the interface of the film by $-\left(1+\frac{2\nu}{1-\nu}\right)\varepsilon_c\cos(\kappa_c x)$ whilst generating no tractions on the free surface. This strain opposes both the stress free strain and the Poisson expansion in the x direction and brings the film back into atomic registry with the substrate.

The correction deformations are plane strain, and since both $\boldsymbol{\varepsilon}^{\mathrm{S}}(x,z)$, and $\boldsymbol{\varepsilon}^{\mathrm{B}}(x) + \boldsymbol{\varepsilon}^{\mathrm{SF}}(x)$ independently satisfy the condition of compatibility then the correction deformations also satisfy the biharmonic equation and can be found by forcing the stress function in (2.19) to meet the boundary conditions described above.

The utility of this (somewhat long winded) approach to finding $\boldsymbol{\varepsilon}^{\mathrm{S}}(x,z)$ and $\boldsymbol{\varepsilon}^{\mathrm{C}}(x,z)$ is that the mean elastic energy density of the film can now be calculated straight forwardly as the sum of the elastic energy of a plane wave heterogeneity in a bulk material plus the work done as the substrate strain and corrective deformations are applied. This procedure yields an elastic energy density

$$\begin{aligned}\langle E_{\mathrm{el}}\rangle &= \langle E_{\mathrm{bulk}}\rangle - a_{cc}(\tilde{h}_c)(1+\nu)^2\varepsilon_c^2 \\ &+ a_{ss}(\tilde{h}_s)(1-\nu)^2\varepsilon_s^2 - \delta_{\kappa_s,\kappa_c}a_{cs}(\tilde{h}_s)(1-\nu^2)\varepsilon_c\varepsilon_s,\end{aligned} \tag{2.23}$$

with $\delta_{\kappa_s,\kappa_c}$ the Kronecker delta, $\tilde{h}_c = h\kappa_c$, $\tilde{h}_s = h\kappa_s$, and

$$\langle E_{\mathrm{bulk}}\rangle = \mu\varepsilon_c^2\frac{1+\nu}{1-\nu}, \tag{2.24}$$

$$a_{cc}(\tilde{h}) = 8W_o(\tilde{h})\sinh^2\left(\tilde{h}/2\right)\left(\tilde{h}+(1-2\nu)\sinh(\theta)\right), \tag{2.25}$$

$$a_{ss}(\tilde{h}) = W_o(\tilde{h})\left(2\tilde{h}+\sinh(2\tilde{h})\right), \tag{2.26}$$

$$a_{cs}(\tilde{h}) = 2W_o(\tilde{h})\left(2\tilde{h}-2\tilde{h}\cosh(\tilde{h})+2(1-2\nu)\sinh(\tilde{h})+\sinh(2\tilde{h})\right), \tag{2.27}$$

$$W_o(\tilde{h}) = \frac{\mu}{\tilde{h}(1-\nu)}\left(5+2\tilde{h}^2-4\nu(3-2\nu)+(3-4\nu)\cosh(2\tilde{h})\right)^{-1}. \tag{2.28}$$

In the limit that the film is very thin in comparison to the interface strain period ($\kappa_s h \to 0$) the mean elastic energy density becomes

$$\langle E_{\mathrm{el}}\rangle \to \frac{\mu}{(1-\nu)}\left(\varepsilon_c^2(1+\nu)+\frac{\varepsilon_s^2}{2}-\delta_{\kappa_s,\kappa_c}\varepsilon_c\varepsilon_s(1+\nu)\right). \tag{2.29}$$

In the limit of the thick film the elastic energy becomes that of the infinite solid in Eqn. 2.24.

2.4.4 Film Stability

2.4.4.1 Linear contributions

An infinitesimal fluctuation will grow if the mean total free energy density of the system ($\langle E_{\rm el}\rangle + \langle F_{\rm TC}\rangle$ from Eqn.s 2.23 and 2.10) is decreased with increasing amplitude. The only contribution to the total free energy linear in ΔC, defined to be $\Delta f_{\rm lin}$, is proportional to $\delta_{\kappa_s,\kappa}$ and is given by

$$\Delta f_{\rm lin} = -a_{cs}(\tilde{h}_s)(1-\nu^2)\varepsilon_s \frac{\Delta V \Delta C}{3}. \tag{2.30}$$

The coefficient $a_{cs}(\tilde{h})$ is positive for all $\tilde{h}$, so the film is unstable with respect to the growth of a composition fluctuation with the same wavevector as the substrate strain. Since the reduction in free energy due to this term is linear in ΔC, this mode is the most unstable during the initial stages of decomposition. Furthermore the instability of the film to first order in ΔC is dictated *entirely* by the elastic properties of the film: chemical contributions to the free energy do not affect this instability. Therefore this instability occurs in all alloy films with $\Delta V \neq 0$ on a strained substrate *regardless of whether or not the bulk system displays a miscibility gap.* Further, this instability can appear at technologically relevant wavelengths smaller that those accessible to chemically driven spinodal decomposition.

2.4.4.2 Quadratic contributions

At all other wavelengths, the stability of the thin film to concentration fluctuations is determined by terms of order ΔC^2. These terms are defined as $\Delta f_{\rm quad}$ and are given by

$$\Delta f_{\rm quad} = \left(\frac{q(\kappa_c)}{4} - a_{cc}(\tilde{h}_c)\,(1+\nu)^2\,\frac{\Delta V^2}{9} \right) \Delta C^2, \tag{2.31}$$

with

$$q(\kappa_c) = f_2 + 2\Gamma\kappa_c^2 + 4\mu \frac{\Delta V^2}{9}\,\frac{(1+\mu)}{(1-\nu)}. \tag{2.32}$$

The film is unstable with respect to the growth of composition waves with wavevector κ_c if the sum in 2.31 is negative, whilst the stability of a bulk solid depends on the sign of $q\,(\kappa_c)$. The only negative term in the simple quadratic equation 2.32 is the constant f_2, so for bulk alloys the infinitely long wavelength mode is always the first to go unstable.

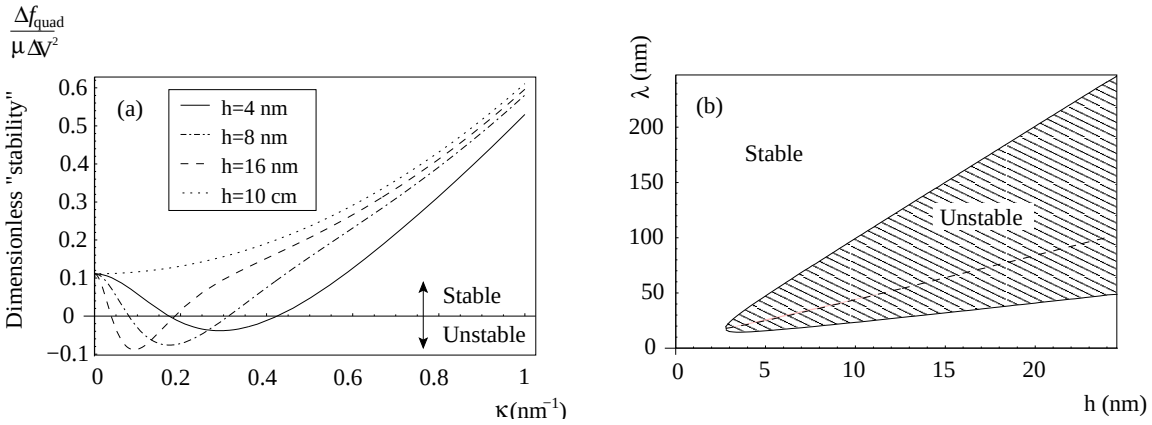

Figure 2.4: Panel (a) Plots of the dimensionless free energy curvature with respect to the growth of a plane wave composition fluctuation with wavevector κ_c nm^{-1} in a film on a rigid unstrained substrate. The films have physical properties $\frac{f_2}{\mu \Delta V^2} = -\frac{2}{3}$ and $\frac{\Gamma}{\mu \Delta V^2} = \frac{1}{2}$ nm^2. These numbers have been estimated using bond counting arguments for a system of two FCC metals near the limit of metastability. In the limit that the film becomes infinitely thick the limits of the domain of unstable wavevectors tend to $\kappa_c = 0$. These unstable modes are kinetically stabilised due to the long diffusion distances involved in their growth. Panel (b) shows the range of unstable wavelengths as a function of film thickness for the same alloy. The dashed line indicates the position of the minima in plot (a).

The function $a_{cc}(\tilde{h})$ is zero in the limits that $\tilde{h} \to \infty$ and $\tilde{h} \to 0$ (the bulk solid and the infinitely thin film[4]), and positive everywhere in between. Based on this it, can be seen from Eqn. 2.31 that alloys which are strain stabilised[5] when in the form of a bulk solid may be unstable when in the form of a film. Segregation in such films arises from the elastic relaxations associated with the free surface.

The domain of unstable surface segregation modes in a film that, as bulk, is strain stabilised is bounded, as demonstrated in Fig. 2.4. St. Venant's principle dictates that the elastic relaxations associated with the free surface decay over the wavelength of the heterogeneity, thus the very short wavelength modes are not unstable because there is comparatively[6] little surface relaxation. The very long wavelength modes are stable because the strain fields from the surface relaxation are cropped by the film thickness. As the film thickness increases the domain of unstable wavelengths becomes wider and longer, so that for a half infinite solid the elastic energy of the very long wavelength modes is reduced relative to those in a bulk solid. This can clearly be seen from the plots in figure 2.4. The

[4]The former case is elastically constrained in the y-z plane whilst the latter case is constrained in the x-y plane.

[5]Here strain stabilised means to have a negative curvature of free energy, f_2, but be prevented from becoming unstable by the elastic strain energy.

[6]The comparison is made with the bulk.

long wavelength modes are, however, kinetically stabilised due to the long diffusion lengths that must be traversed during their growth.

It is reasonable to expect that a closed domain of unstable modes will also be observed when the rigid substrate constraint is relaxed, and the compatibility strain field penetrates the substrate. In this case, although the surface strain fields are no longer truncated by the substrate, the driving force for segregation is limited by the film thickness.

2.5 Extent of segregation

Simply knowing that an alloy film will segregate is not sufficient for deciding if a film is a suitable precursor for producing self-assembled nanostructures. It is also necessary to understand the extent to which segregation will occur and the relative amplification rates for composition fluctuations with different wavelengths. The driving force for the evolution of a composition fluctuation is the variation in the mean total free energy, $\langle \delta f_{\rm tot} \rangle$, that accompanies a variation in the concentration, $\delta C(\boldsymbol{r})$. Following Cahn the general form of this variation is written as

$$\langle \delta f_{\rm tot} \rangle = \int_V \frac{1}{V} \left[f_1 + f_2 \tilde{C} - 2\Gamma \nabla^2 \tilde{C} + \frac{\delta \mathcal{F}_{\rm el}\{\tilde{C}\}}{\delta \tilde{C}} \right] \delta \tilde{C} dV, \tag{2.33}$$

where the composition distribution is given by $C(\boldsymbol{r}) = C_o + \tilde{C}(\boldsymbol{r})$. The term in brackets in Eqn. 2.33 is the chemical potential, $\eta(\boldsymbol{r})$, so if it is assumed that the evolution of the composition distribution is diffusion mediated then the change in concentration with time is given by the diffusion equation $\frac{\partial \tilde{C}}{\partial t} = \nabla \left(M \nabla \eta(\boldsymbol{r}) \right)$.[7] Here M is a mobility coefficient (assumed isotropic) chosen to be independent of concentration. The diffusion equation must be solved such that the change in concentration with time is consistent with the variation in concentration for which $\eta(\boldsymbol{r})$ is calculated (Eqn. 2.33). In general the assumed form for the composition fluctuation does not satisfy this requirement, and one cannot predict the early time amplification rate of the unstable modes presented above.

In the limit that the film is very thin (in comparison to the wavelength of a composition fluctuation) the elastic energy Eqn. (2.29) tends to that of a film in which there is no z component of the strain. In this limit the elastic energy density is no longer a functional

[7] It is more common to express a chemically driven flux $-M'C\nabla\eta(\boldsymbol{r})$ where the mobility $M' = D\beta$ (with D the diffusion coefficient, β the reciprocal thermal energy. Here, however, it is assumed the $C_o \ll \tilde{C}$(r), and so the concentration is incorporated into the mobility M.

of the whole concentration distribution but only depends on the *local* concentration as the film is fully constrained by the substrate. Now the assumed form of the composition fluctuation (Eqn. 2.8) becomes meaningful, and one can solve for the early time (*i.e.*, linear) amplification rates.

The diffusion equation for the thin film is rewritten

$$\begin{aligned} \frac{\partial \tilde{C}}{\partial t} &= M\left(f_2\nabla^2\tilde{C} - 2\Gamma\nabla^4\tilde{C}\right) \\ &+ \frac{2}{3}M\mu\Delta V\frac{(1+\nu)}{(1-\nu)}\left(\frac{2\Delta V}{3}\nabla^2\tilde{C} + \varepsilon_s\kappa_s^2\cos(\kappa_s x)\right). \end{aligned} \tag{2.34}$$

Solving Eqn. (2.34) subject to the constraint that the film decompose only in the x direction gives

$$\begin{aligned} \tilde{C}(t,x) &= \varepsilon_s\frac{(1+\nu)}{(1-\nu)}\frac{\mu\Delta V^2}{q(\kappa_s)}\cos(\kappa_s x)\frac{2}{3}\left(1 - e^{-M\kappa^2 q(\kappa_s)t}\right) \\ &+ \int_{-\infty}^{\infty} d\kappa_c \phi_{\kappa_c} e^{i\kappa_c x} e^{-M\kappa_c^2 q(\kappa_c)t}, \end{aligned} \tag{2.35}$$

where ϕ_{κ_c} is the κ_cth Fourier component of the initial concentration distribution. As is the case with a bulk solid *all* fluctuations with $q(\kappa_c) < 0$ will grow exponentially until the assumed linearity is no longer valid. Fluctuations with $q(\kappa_c) > 0$ will decay to zero with the exception of the fluctuation in phase with the substrate strain that approach a steady state amplitude:

$$\tilde{C}(\infty, x) = \varepsilon_s\frac{(1+\nu)}{(1-\nu)}\frac{\mu\Delta V^2}{q(\kappa_s)}\cos(\kappa_s x)\frac{2}{3}. \tag{2.36}$$

An estimate of the amplitude of this fluctuation for a material in which bulk spinodal decomposition is inhibited by the elastic strain indicates that the steady state amplitude of this concentration wave can be large enough to invalidate the linear assumptions made here. So, the effect is expected to be significant.[8]

The analysis presented here is deterministic and does not contain noise. If the film is initially homogeneous this model predicts that the *only* mode that grows is the mode that relaxes the strain imposed by the substrate.

Finally, it should be noted that only a single Fourier component of the substrate strain was considered. It can now be seen that if the substrate has a long period with a more abrupt change in strain[9] then the strain will contain Fourier components with short

[8] Values for Γ and f_2 were estimated for a typical immiscible FCC metal alloy by bond counting arguments following Khachaturyan [29].

[9] This could be achieved by lithography, or by slicing multilayer structure at a glancing angle.

wavelengths. It can be seen by integrating equation 2.35 that the early time amplification rate of a given mode is proportional to the square of its wavenumber. Hence, the combination of fast development of short wavelength modes and the effect of Gibbs overshoot could allow uniform fine-scale structures to be grown from a large scale lithographic pattern.

2.6 Summary

In this chapter the calculation of the residual strain on the surface of a misfit dislocated film was presented. It was then demonstrated that, in theory, alloy films homogeneously deposited on such a film will segregate, and that initially the most unstable heterogeneity has a wavelength determined by the periodicity of the substrate. It was also shown that films may also be unstable to the considered fluctuations in the absence of a periodically strained substrate. Under these circumstances, the unstable wavelengths are bounded and may be as short as tens of nanometres. While there may be concentration fluctuations more unstable than those considered here, the current calculation establishes rigorously the instability of some thin films to spinodal decomposition at the nanometre scale. In the thin film limit, the assumed form of the composition fluctuations is the expected form, and the linear amplification rates can be obtained. In summary, it appears that spinodal decomposition in the presence of a periodic strain is a viable candidate for the self-organised growth of nanostructures.

Chapter 3

Nucleation and growth of islands during epitaxial film deposition

3.1 Introduction and background

In the previous chapter it was demonstrated that a strain pattern will lead to segregation in an alloy film. However, strain will also influence the deposition and growth of a film. In this chapter some issues arising during the early stages of deposition and growth of an epitaxial film on a strained substrate are examined.

When an epitaxial film is grown by physical vapour deposition (PVD) atoms arrive at the substrate surface individually and move around on it randomly. Initially the concentration of lone atoms rises. The free energy of this sea of adatoms is reduced by the aggregation of monomers to form an archipelago of adatom clusters or "islands." Once these clusters have been nucleated, additional atoms arriving at the surface are more likely to encounter an island than another diffusing monomer. Thus, existing islands grow with little further nucleation of new island. Eventually these islands coalesce and a contiguous film is formed. Surface strain impacts both the *thermodynamic* driving force for aggregation to islands and the *kinetics* that mediate it.

The strain from a network of misfit dislocations was calculated in section 2.3 where figure 2.2 shows the variation in the trace of the surface strain tensor across the substrate. The adsorption energy of an adatom on the surface of a substrate (the energy required to remove the atom from the surface) is a scalar property, that, at least to first

order, is proportional to the trace of the surface strain. Applying such an interpretation to figure 2.2 reveals a (local equilibrium) potential energy surface with a regular array of low energy basins, and thus thermodynamically preferential zones for clustering of adatoms. The surface mobility of an adatom on the other hand is a tensor property and so depends on the whole surface strain tensor, and possesses the same symmetry as the deformed crystal. This means that in plots (a) and (b) of figure 2.2 near the tops of the hillocks and the bottoms of depressions the mobility will be different but isotropic, whilst in the saddle regions the kinetics of transport will be anisotropic. Moreover it is not known *a priori* in which regions the kinetics will be fastest, nor if there will be a change in the dominant diffusion mechanism from region to region.

The topic of this chapter is the effect of strain and its influence on transport kinetics. Consideration is limited to homoepitaxy on the (001) surface of FCC metals. FCC metals do not have strong angular bonding. These surfaces are square lattices that have isotropic diffusivities, and for the most part, do not reconstruct (Au, Pt, and Ir being among the exceptions). The seeming simplicity of these systems makes them a good starting point to investigate some of the subtle behaviour that arises due to strain. A possible new mechanism for surface diffusion–the surface crowdion–is outlined, and the implications of this transport mechanism for the early stages of film growth are examined qualitatively. The ultimate goal of the remainder of this thesis is to determine if the surface crowdion, that so far has only been predicted to exist theoretically, can be observed experimentally through island growth experiments.

3.1.1 Strain, diffusion, and surface crowdions

It is widely understood that diffusion on FCC (001) metal surfaces happens by one of two mechanisms;[1] a simple hop one atom spacing in a $\langle 110 \rangle$ direction, or a displacive reaction one lattice parameter in the $\langle 100 \rangle$ direction. Cartoons of these processes are shown in figure 3.1. In the displacive mechanism the diffusing adatom sinks into the surface and replaces one of the nearest neighbour substrate atoms which, in turn, is "kicked out" to the surface. In the case of homoepitaxy, as the atoms are indistinguishable, it may be considered

[1] There have been theoretical studies that found low energy barriers for more complicated diffusion mechanisms, however, the calculated energy barriers are not as low as those for the mechanisms considered here, nor is there any experimental evidence for them [30, 31].

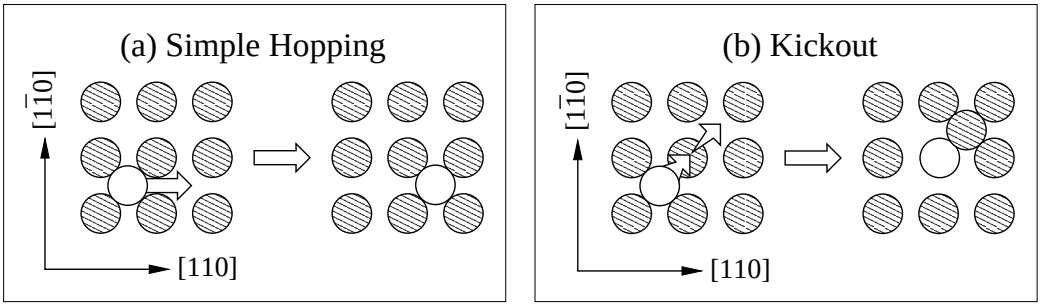

Figure 3.1: Cartoons of surface diffusion mechanisms on FCC (001) metal surfaces. Panel (a) depicts simple hopping whilst panel (b) shows the displacive "Kickout mechanism. In both diagrams the hatched circles depict the original (001) surface atoms while the unshaded circle depicts the original adatom. The two diagrams show the atom positions before and after the mechanism has occurred.

that the original adatom has hopped diagonally.[2] A consequence of the diagonal movement is that an adatom diffusing by "kickout" is restricted to visiting a sublattice of surface sites in the same way that a bishop in a game of chess must remain on the same colour squares that it started on. It is known, based on theoretical predictions of Feibelman [32], Boisvert and Lewis [33], Xiao *et al.* [34] and Mehl *et al.* [30], and detailed experiments by Kellogg [35] (measuring site visitation maps by field ion microscopy), that Cu on Cu diffuses by the hopping mechanism, whilst Al on Al diffuses by the displacive mechanism. Recent theoretical work by Xiao, Greaney and Chrzan [34], and Voter *et al.* [36] however, shows that the energy barriers for both of these mechanisms respond differently to strain and that by straining Cu it is possible to switch the dominant diffusion mechanism from hopping to kickout. Moreover in their work Xiao *et al.* discovered that highly non-tetragonally strained Cu could exhibit a new adatom transport mechanism–a surface crowdion.

The surface crowdion is a metastable surface defect (shown in figure 3.2) in which an adatom is absorbed into a close packed atomic row in the substrate. The extra atom is accommodated in the surface by 8 or 10 atoms in a single atomic row all shuffling along that row. The row along which the displacements are extended lies in the $\langle 110 \rangle$ direction with the least compressive strain, hence in a homogeneously strained material all crowdions will be extended in the same direction. Crowdions in bulk materials were hypothesised as a diffusion mechanism in the 1950s. However, there is little experimental evidence for them

[2]This is only applicable when the atoms are quantum mechanically indistinguishable, *i.e.*, in self-diffusion. The rate of transport of tracer atoms will be very much lower that the rate of self-diffusion.

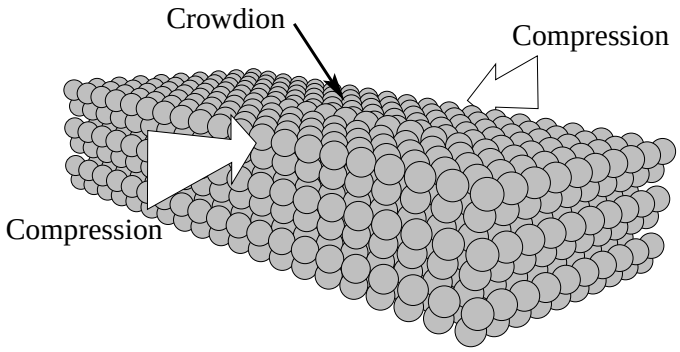

Figure 3.2: Perspective picture of a crowdion on the (001) surface of Cu. Atom positions were calculated using NEB and EAM by Xiao *et al.* [34]. Arrows indicate the direction of compressive strain.

with the exception being in radiation damaged materials where the existence of crowdions is inferred from transmission electron microscopy studies of vacancy clusters sizes, and internal friction experiments [37, 38].

Xiao *et al.* predict the structure of the surface crowdion in Cu by using the nudged elastic band method (NEB) to explore phase space[3] for a minimum energy trajectory between the initial and final configurations of the kickout mechanism shown in panel (b) of figure 3.1. They calculate the energies of configurations in phase space using the embedded atom method (EAM), an empirical potential suited to calculating the total energy of configurations of large numbers of FCC metal atoms. The strain at which they calculate the crowdion to be come the low energy diffusion mechanism is large; a 2% uniaxial strain in the plane of the surface.

In a single component system, once a crowdion is formed, it is not possible to distinguish the original adatom from the other atoms at the centre of the crowdion. Only by looking at the distribution of atomic displacement along the close packed row does the crowdion make itself apparent, thus the crowdion may be considered a quasiparticle that carries one quantum of "atomic displacement" parallel to the row. Figure 3.3 shows the atomic displacements along a crowdion row in Cu. It can be seen that the displacements are distributed over approximately 10 atoms. Moving the centre of the crowdion one atom spacing along its extended direction involves only small changes in the individual atom displacements, thus the energy barrier for moving the crowdion along its row is very small

[3]Phase space here is the $3N$ space defined by the coordinates of the N atoms.

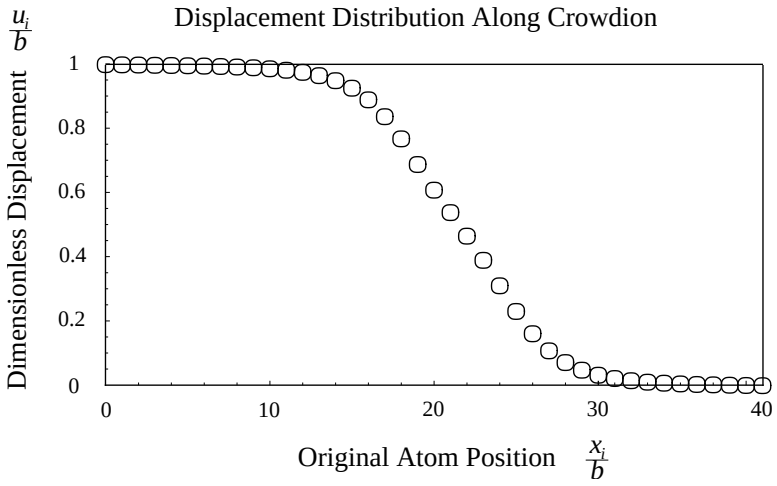

Figure 3.3: Plot showing the dimensionless displacement of Cu atoms along the crowdion row calculated by Xiao.

($O(0.001)$ eV, less than thermal energy at room temperature). The energy required to move the crowdion from one row to an adjacent row, however, is larger than the decay energy of the crowdion.

3.2 Crowdion motion

As the surface crowdion is metastable, has little or no barrier to moving, and carries a unit of atomic displacement it would seem that, in *single component systems*, crowdions would mediate rapid self diffusion. If crowdions exist in alloys they would *not* provide a mechanism for long range intermixing, but they would provide a mechanism for rapid mass transport. That is they would allow a material to creep quickly in response to an applied stress but would not allow rapid segregation. Moreover as the total population of crowdions are only mobile in one direction, crowdions would mediate highly anisotropic diffusion. It is argued in this section that the crowdion may provide a long range *self*-diffusion mechanism.

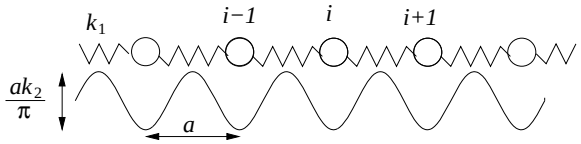

Figure 3.4: The Frankel-Kontorova model considers the motion of a chain of atoms connected by springs of strength k_1, sitting in a potential of amplitude $\frac{k_2 a}{2\pi}$ and wavelength a.

3.2.1 Crowdion kinetic energy and effective mass

The kinetic energy of a moving crowdion is the sum of the kinetic energy of all atoms that are displaced as the crowdion moves

$$E_k = \frac{1}{2} m^* v_c^2 = \sum_i \frac{1}{2} m \dot{\boldsymbol{u}}_i^2. \tag{3.1}$$

Here m is the atomic mass, m^* is the effective mass of the crowdion, v_c is the velocity of the crowdion, $\boldsymbol{u}_i$ is the displacement of the ith atom, and the sum is performed over all the atoms in the crowdion. The problem of a moving crowdion can be represented by the Frankel-Kontorova model [39, 40]. This model considers the displacement, u_i, of the ith atom in a one dimensional chain of particles connected by spring (of strength k_1) sitting in a sinusoidal potential (of amplitude $\frac{ak_2}{2\pi}$ and wavelength a) as shown in figure 3.2.1. The equation of motion of the continuous form of this problem is the sine-Gordon equation which has travelling kink and antikink solutions of the form

$$u(x,t) = \frac{2}{\pi} \arctan\left(\pm \exp\left(\frac{2\pi k_2}{k_1 - \rho v} \right)^{\frac{1}{2}} (x - vt) \right). \tag{3.2}$$

This is the equation of a soliton moving with a velocity v_c through a medium of density ρ.[4] The shape of the soliton does not change as it moves but it becomes narrower as $v \to \frac{k_1}{\rho}$. It is found numerically that the solution changes very little when the problem is discretised (*i.e.*, atoms are reintroduced), and so as a first approximation it may be assumed that a crowdion moving at low (sub relativistic) velocities maintains a constant shape. Making this approximation allows the velocities of the atoms in the crowdion to be estimated to first order as

$$\dot{\boldsymbol{u}}_i \approx (\boldsymbol{u}_i - \boldsymbol{u}_{i-1}) \frac{v_c}{b}, \tag{3.3}$$

[4]It should be noted that there is *no* energy barrier for moving the soliton, and the energy barrier for the discretised problem, calculated numerically, is extremely low. This adds credibility to Xiao *et al.*'s claim that they cannot resolve the energy barrier for crowdion motion using the embedded atom method.

where b is the equilibrium atom spacing along the crowdion direction (and the net displacement carried by the crowdion, analogous to the Burgers vector of a dislocation). Substituting this into 3.1 leaves the effective mass of the crowdion as

$$m^* = m \sum_i \frac{(\boldsymbol{u}_i - \boldsymbol{u}_{i-1})^2}{b^2}. \tag{3.4}$$

Applying this formula to the computed crowdion structures for Cu gives the effective mass for the crowdion in Cu $\frac{m^*}{m} = 0.071$. More intuitively one can see that if the displacement is spread more or less uniformly over n atoms then the ratio of effective mass to atomic mass must be on the order of $\frac{1}{n}$.

3.2.2 Non-diffusive kinetics

Based on the low energy barrier for moving a crowdion in comparison to its decay energy, and because of the small effective mass of the crowdion, it is hypothesised that the surface crowdion may be "born" with some kinetic energy. That is, some fraction of the potential energy that the system must posses as it passes through the transition state on its way to forming a metastable crowdion is converted to kinetic energy of that crowdion (the rest excites phonon modes). Such an occurrence would give the crowdion a large initial velocity when it is formed and implies that the motion of the crowdion itself is non-diffusive.

Calculating what fraction of the saddle point potential energy might be converted to kinetic energy is nontrivial. However, one can estimate the crowdion velocity by assuming that it posses kinetic energy of the order of the thermal energy. Based on this it is found that a crowdion in Cu at room temperature will move at ~ 750 ms^{-1}. While still subsonic, the large magnitude of this speed indicates that a more elaborate calculation of the crowdion speed is needed, a calculation in which relativistic effects and phonon radiation are accounted for. The simple calculation does, however, indicate that crowdion velocities can be substantial.

Classical solitons pass through each other without effecting each other but it is not known *a priori* how colliding crowdions interact. Xiao has shown [41], however, that the decay energy of a crowdion is reduced when it encounters a second adatom or island on the surface.

The arguments outlined above can be combined into a model of how crowdions might mediate self-diffusion on a homogeneously strained FCC (001) Cu surface. In this

model, a crowdion, once born, will shoot off in one direction radiating phonons as it goes. It will travel, on average, some characteristic distance until it is scattered and or decays. The mean displacement between where a crowdion is created and where it decays will be depend on the phonon scattering, temperature, and the decay free energy of the crowdion. Should the crowdion encounter any surface adatoms or islands it is assumed to decay and eject an atom to the surface which binds to the surface feature.

3.2.3 Diffusion mediated by surface crowdions

The above model of crowdion motion implies a coarse-grained picture in which the self-diffusion of an adatom by crowdions alone is similar to that of a one dimensional random walk making large jumps on a lattice. In this analogy the crowdion's bursts of motion are akin to the walker jumping large numbers of lattice spacings in each step, with a distribution of step lengths centred around a mean step size. The walker is considered to have "visited" or sampled each site it passes through between its initial and final position in each jump. The real crowdion is slightly more complicated than this, because of the A-B-A-B stacking sequence in the (001) direction of FCC lattices. The crowdion's atomic row *in* the surface lies between two rows of lattice sites *on* the empty surface. When a crowdion decays it ejects an atom to the surface the new adatom must sit in one of the vacant surface sites on either side of the crowdion row. Since the crowdion is metastable, the direction in which symmetry is broken when the crowdion decays is not coupled to the original position of the adatom that created the crowdion. In this way the crowdion can mediate diffusion normal to its direction of travel. The second consequence of the A-B-A-B stacking is that the crowdion samples each of the surface lattice sites it in the two parrallel rows as it moves between in each jump.

The macroscopic diffusion tensor, $\boldsymbol{D}$, is related to the microscopic diffusion processes by [42]

$$\boldsymbol{D} = \frac{1}{2} \sum_i \left(\boldsymbol{r}_i \otimes \boldsymbol{r}_i \right) R_i, \tag{3.5}$$

where $\boldsymbol{r}_i$ is the displacement vector, and R_i is the rate of the ith jump process. The sum is performed over all possible diffusion processes. For the case of surface diffusion in which adatoms move in the x and y directions by hopping at rates of R_x and R_y, and crowdions

(extended in the x direction only) are created at a rate R_c the diffusion tensor is

$$\boldsymbol{D} = \frac{a^2}{4} \times \begin{vmatrix} \left(R_x + d_c^2 R_c\right) & 0 \\ 0 & \left(R_y + \frac{R_c}{2}\right) \end{vmatrix}. \tag{3.6}$$

Here d_c^2 is the mean squared number of lattice sites the crowdion jumps before decaying, and a is the FCC lattice parameter. It can be seen that even if the rate of crowdion formation is two orders of magnitude lower than the hopping rates, crowdions can impact the diffusion tensor because the displacement term enters squared.

The quadratic dependence on the jump length is of particular importance. On the microscopic level it means that a small number of "big" events can be of equal importance as a very large number of small events, a principle which is the essence of the Weierstrass random walk.[5] The practical benefit is that it may be possible to detect the existence of crowdions from diffusion experiments *without* having to create 2% uniaxially *elastically* strained Cu films, a task that could prove challenging.

3.3 Detecting crowdions

Thus far crowdions have only been "seen" in embedded atom calculations, so establishing their existence *experimentally* is of utmost importance. This task is fraught with difficulties, the first of which is producing substrates with the strains under which crowdions appear. This can certainly be done in small areas (from misfit dislocations say) but is more tricky for large area studies[6].

3.3.1 Direct observation

Should such substrates be created the high mobility of crowdions would probably make them invisible to invasive surface characterisation techniques such as scanning tunnelling microscopy (STM) and atomic force microscopy (AFM). As crowdions locally disrupt the translational symmetry of the lattice it is reasonable to expect that crowdions, if they exist, will affect surface diffraction patterns produced from low energy electron diffraction (LEED), and low energy He ion scattering.

[5] A Weierstrass random walker makes jumps of variable length where order of magnitude larger jumps occur with order of magnitude lower frequency [43].

[6] It would require growing Cu on a tetragonal or orthorhombic substrate with its c axis in the plane of the interface.

3.3.2 Tracer diffusion

The most obviously noticeable effect of crowdions is that the original surface adatom is not the one which is transported. This will be apparent in a tracer diffusion experiment in which a radioisotope of Cu is deposited on naturally occurring Cu. Isotopes ^{61}Cu, ^{64}Cu, and ^{67}Cu have halve lives of 3.3 hours, 12.7 hours, and 2.5 days and decay to ^{61}Ni, ^{64}Zn, and ^{67}Zn respectively.

Comparing the extent to which surface adatoms have travelled, and the extent to which the decay products of the radioisotopes (Ni and Zn) have moved will reveal if the diffusion is occurring by a displacive mechanism such as the kickout or the crowdion. If the islands of adatoms on the surface contain predominantly naturally occurring Cu then the diffusion mechanism is most likely displacive. The two displacive mechanisms can be distinguished by looking at site visitation, or anisotropy. If the crystal is strained such that the square lattice of surface sites becomes rectangular (*e.g.* uniaxial strain in the $\langle 110 \rangle$ direction), then the kickout mechanism remains isotropic (in the frame of reference of the undistorted lattice) whilst crowdion formation is inherently anisotropic. Alternatively one could observe the set of sites visited by a diffusing adatom. Kickout diffusion is restricted to a sublattice empty surface sites whilst crowdion diffusion is not.

3.3.3 Island growth and quasi-hexagonal reconstruction

It is possible that evidence of the long-range crowdion diffusion mechanism hypothesised above will affect island growth phenomena. To investigate this one can proceed phenomenologically and determine the implications of the long-range mechanism on island nucleation and growth. The aim is to determine if crowdions give rise to discernibly "different" island growth than would occur with just highly anisotropic hopping. Such a scenario could lead to experiments which either corroborate the existence of *crowdions*, or refute that this *mechanism* of transport occurs (*N.B.* a negative result of such an experiment does not rule out the existence of crowdions, only the method by which they are hypothesised to move). This is the topic of the rest of this thesis.

Using EAM Xiao has predicted metastable crowdions in Cu and Pt but not in Al. Pt along with Au and Ir exhibit a quasi-hexagonal surface reconstruction [44, 45, 46, 47, 48] in which the (001) surface becomes terminated by atoms resembling a (111) plane. The reconstruction is shown schematically in figure 3.5. An extra row of atoms is inserted into

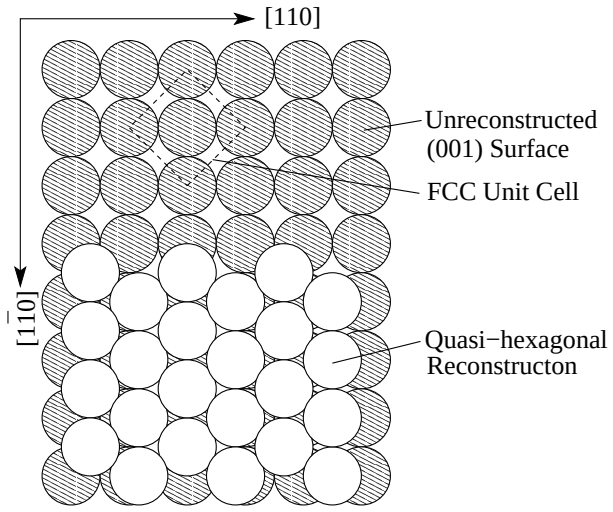

Figure 3.5: Schematic representation of the quasi-hexagonal reconstruction on a (001) FCC surface. The hatched circles represent the unreconstructed (001) surface. The unhatched circles represent the $i \times 5$ reconstructed layer. The unit cell of the FCC lattice is shown with dotted lines. The areal density of atoms in the reconstructed layer is $\sim 20\%$ greater than the unreconstructed layer.

the surface in the $[1\bar{1}0]$ direction for every 5 rows in the [110] direction of the unreconstructed surface. To accommodate the strain, alternate $[1\bar{1}0]$ rows shuffle half an atom spacing in $[1\bar{1}0]$ giving the atoms a hexagonal coordination, and generating six atom wide corrugation on the surface. The $[1\bar{1}0]$ direction of the reconstructed layer does not remain commensurate with the lattice below it but an extra atom is added to every $[1\bar{1}0]$ row for every i atoms in the row. The reconstructed layer is only commensurate with the underlying lattice every i atoms in the $[1\bar{1}0]$ direction. For Pt and Au i=25 and 34, respectively [47, 48].

Both diffusion and island growth on the hexagonally reconstructed surfaces are found to be highly anisotropic [48, 49] with very fast diffusion in the $[1\bar{1}0]$ direction. Linderoth and coworkers measure the ratio of diffusion coefficients in the fast and slow directions to be on the order of 10^3 at room temperature. This is surprising given that the surface, at least to first approximation, is hexagonal! The anisotropy is attributed to the surface corrugation [44, 49], however, to date no satisfactory explanation of how the corrugation influences diffusion has been given.

The extra atom every i atoms in each of the $[1\bar{1}0]$ rows forms a soliton like structure [47]. Although the structure of these solitons is very different from the crowdion in the unreconstructed surface they might be expected to mediate diffusion with the same

long jumps that are hypothesised for (001) crowdions. Hence, studying this type of diffusion phenomenologically may provide insight to diffusion on FCC (001) quasi-hexagonally reconstructed surfaces.

3.4 Island growth

3.4.1 Background

In the early stages of epitaxial film growth adatoms muster into small groups. This happens regardless of whether the film grows by Frank-Van der Merwe growth, Volmer-Weber growth, or Stranski-Krastanov growth[7]; at some point the film must be nucleated. It is easy to see that there must be some critical size, i, of these clusters such that the free energy of the system is reduced if one atom leaves a cluster of i atoms but if an atom joins a cluster of $i+1$ atoms the energy of the system is also reduced.[8]

Nucleation and growth of films has been studied extensively both experimentally and theoretically. Theoretically the problem of nucleation on a substrate is simpler than the nucleation of a solid from a melt. In this case, since atoms can only occupy fixed positions on the substrate surface one need not worry about Lothe-Pound [50] corrections, and issues of heterogeneous versus homogeneous nucleation are meaningless. Besides the obvious technological relevance of studying film nucleation, it has gained further importance because of advances in atomic-resolution surface characterisation techniques (such as STM), and numerical "experimentation" methods. These methods allow direct comparison between the rate equation descriptions of aggregation and real or numerical experiments. Together these tools have lead to a good understanding of the early stages of film growth.

3.4.1.1 Rate equations

Nucleation and growth of critical clusters of atoms during the precoalescent stages of film deposition is just one of a variety of aggregation phenomena that includes colloid formation, blood clotting, aerosol formation, gelation, and polymerisation. The first theoretical description of these general class of phenomena was given by von Smoluchowski in 1916 [51], who described the temporal evolution of an aggregating system with a set of

[7]These correspond to layer by layer growth, three dimensional island growth, and layer by layer growth followed by islanding.

[8]This assumes all clusters are the same shape, and strain is unimportant.

coupled rate equations. In this set of equations the rate of change in the population of each sized aggregate is dependent on the populations of aggregates of other sizes. The equations can be made as complicated or as simple as required to account for the interactions occurring in the system in question.

Irreversible nucleation and growth of films–where the critical cluster size i is 1–can be represented by one of the simplest, non-trivial, manifestations of von Smoluchowski's rate equations. During irreversible growth it is assumed that atoms are continually deposited on the substrate with a flux, F. The deposited atoms do not desorb. Only free monomers (whose mean number density is defined as $\langle n_1 \rangle$) are deemed to be mobile. In the case of isotropic diffusion the rate of change in the mean density of clusters of size s is given by

$$\frac{d\langle n_s \rangle}{dt} = F\Big(p_{s-1}\langle n_{s-1}\rangle - p_s\langle n_s\rangle\Big) + D\Big(\sigma_{s-1}\langle n_{s-1}\rangle\langle n_1\rangle - \sigma_s\langle n_s\rangle\langle n_1\rangle\Big), \tag{3.7}$$

where $\langle n_s \rangle$ is the mean number density of clusters of s atoms averaged over the whole substrate. In Eqn. 3.7 the first two terms account for the addition and subtraction of island of size s due to the direct impingement of atoms from the vapour with islands of size $s-1$ and s respectively. The coefficient p_s is the direct capture cross section of a island of size s to vapour atoms. How p_s varies with s depends on the geometry of the island.[9] The second two terms account for the growth of islands by aggregation of monomers, and so must be dependent on the mean density of monomers and the diffusion coefficient, D. The set of dimensionless coefficients, σ_s, are the "capture numbers" which denote the ability of an island of size s to capture diffusing monomers.

The rate of change of the average monomers density is a little more complicated and is given by

$$\frac{d\langle n_1 \rangle}{dt} = F\left(1 - 2p_1\langle n_1\rangle - \sum_{s\geq 2} p_s\langle n_s\rangle\right) - \left(2\sigma_1\langle n_1\rangle^2 + \sum_{s\geq 2}\sigma_s\langle n_s\rangle\langle n_1\rangle\right). \tag{3.8}$$

Here the terms in the first parentheses account for direct flux of adatoms from the vapour. The terms in the second parentheses are the loss of monomers on the surface by either aggregation to existing islands or nucleation of a new island by the collision of two monomers.

The detailed physics of a particular aggregation phenomena lie in the innocuous looking capture numbers. Venables [52], and Bales and Chrzan [2] developed a self-consistent method for calculating the capture numbers for the case of layer by layer growth

[9] Whether islands are two dimensional or three dimensional, and whether they are fractal, dendritic, or compact.

where the islands remain two dimensional as they grow. In this case the rate equations can be made dimensionless by considering the rates of change of population densities with respect to the area of the substrate that had been covered. Bales and Chrzan found the rate of capture of monomers by solving, self-consistently, the diffusion equation for the local density of monomers in a mean field of monomer sinks (islands) and sources (the flux).

A simplified rate equation approach was originally solved self consistently by Venables [53] who lumped the populations of all supercritical islands together into a single population density $\langle n_\chi \rangle$.

Evans and Bartelt [54] have integrated the same reduced set of rate equations analytically by assuming asymptotic forms for the capture numbers based on the number of unique sites visited by a random walker and assuming the islands to be points. These researchers have in the same way integrated these equations for the case of purely one dimensional diffusion on a two dimensional substrate.

Once islands have been nucleated they act as sinks depleting the monomer concentration around them. Since the probability of nucleating an island goes as the square of the monomer density, further nucleation events are not distributed uniformly on the substrate but are more likely in the spaces between islands where the monomer concentration is highest. This has been elegantly demonstrated using level set simulations by Ratsch and coworkers [55]. The rate equation description of island growth is a mean field approximation, and hence does not capture the correlation effects of nucleation. So, while the rate equation formulation captures the evolution of the total number density of islands and some of the scaling phenomena, it fails to predict the distribution of island sizes.

Recently Popescu, Amar, and Family [56, 57, 58] have developed a mean field rate equation description that does predict the observed island size distribution. Popescu and coworkers consider the depleted regions (or Voronoi cells[10]) around the islands. They assume that the population of islands of size s resides in a distribution of differently sized Voronoi cells. Then, they not only consider the evolution of the island populations but also the evolution of the distribution of sizes of cells that they occupy. They effectively make the capture numbers, σ_s, depend on the whole distribution of island separations, and then solve for them self-consistently.

[10]The Voronoi cell of an island is the locus of points closer to that island than any other. This is the polygon who's edges are the perpendicular bisectors of the inter-island vectors.

3.4.1.2 Numerical simulation

The aim of simulating film growth is neither to predict quantitatively the outcome of a particular set of growth parameters, nor to replicate all the complexities of film growth. Rather, simulation is a tool that allows insight to be gained by constructing simple models that display experimentally observed phenomena. It is a direct way of finding the consequences of a hypothetical set of interactions. At the same time one must be wary that simulations are not a palimpsest, that is not devised or revised, so as to give the desired result without consideration of other interactions that could either also give the same behaviour, or destroy it. Building a useful KMC model requires striking a balance between encompassing enough complexity so that its behaviour is not obvious *a piori*, whilst not making the simulation so complicated that physical insight is obscured.

As nucleation and growth is an inherently stochastic process occurring far from equilibrium the kinetic Monte Carlo (KMC) algorithm is the most commonly used method for simulating it. A KMC simulation follows the individual jumps of a collection of atoms on a substrate. All possible "events" (in this case atomic jumps) are enumerated and assigned a rate R_i. At each iteration of the algorithm the possible events are weighted by their relative rates, $\tilde{R}_i = \frac{R_i}{\sum_j R_j}$, then one is selected at random and made to occur. After each step the rates are reevaluated and the elapsed time is advanced with the stochastic interval $\Delta t = \frac{1}{\sum_j R_j} \ln\left(\frac{1}{\zeta}\right)$, where ζ is a positive random fraction. This time step gives a Poisson distribution of intervals between events with an expectation value of $\langle \Delta t \rangle = \frac{1}{\sum_j R_j}$. The physics of the system being simulated is contained in the "events" that are allowed to occur and the rates that are assigned to them.

The rate with which an adatom performs various jumps depends on its local environment, that is, the local strain, and the number and configuration of the nearest and next nearest neighbours. KMC simulations generally assign rates of hopping by one of two schemes. The first is a bond counting scheme in which the energy barrier for the ith event, E_i, is assumed be some function of the number of neighbours before and after the event. A uniform "attempt frequency", ω, is assumed and the rate of the ith event is given by the Boltzmann distribution $R_i = \omega e^{-E_i \beta}$, with β the reciprocal thermal energy. Detailed balance[11] is obeyed by simply ensuring that the difference in the energy barrier between the forward and reverse processes is the same as the difference in energy between the initial

[11] Detailed balance is the requirement that there be no closed cycle of events which changes the total energy of the system; to do so would violate the first law of thermodynamics.

and final configurations. The advantage of this scheme is that it is easy to implement. However, the validity of the bond counting argument is suspect, especially for atoms hopping at island edges. A second scheme is to generate a lookup table of allowed events and their rates (or energy barriers) for different configurations of adatoms. The rates or energy barriers or processes with different atomic configurations can be calculated (or measured) separately using *ab initio* techniques or empirical methods. Alternatively simulations can be performed as phenomenological numerical experiments in which rates are assigned to a lookup table of events with no detailed physical justification, the aim being to see what would be the consequence of such a scenario. The KMC experiments documented in this thesis fall into this last category.

Almost every theoretical or experimental work on the nucleation and growth of islands is accompanied by some form of KMC simulation. Bales and Chrzan [2], Family *et al.* [56, 59], and Evans and Bartelt [54] all compare predictions of their rate equation analysis to simple KMC simulations, while Kern *et al.* [9], and Linderoth *et al.* [49] all compare STM studies to idealised KMC simulations.

Romanov and Speck [5], Sabiryanov *et al.* [7], Larsson *et al.* [6, 8] have performed KMC simulations of the growth and ordering of islands on (111) and (001) FCC surfaces that are periodically strained by misfit dislocates. This body of work sets out to determine the optimum growth parameters to obtain nanoscale patterning and, like all good KMC studies, they oversimplify the processes involved. In particular they only consider the trace of the strain tensor as the important parameter.

Islands of adatoms grown epitaxially will impart a strain (which decays as $\sim r^{-3}$) in the substrate upon which they reside (even homoepitaxial islands). Thus, a complete simulation of island growth would incorporate the strain on the substrate, updating the strain field every time an atom moves and then recalculating the hopping rate for every atom based on the new strain. This procedure becomes exorbitantly costly in computer time for any practical simulation and so most researchers (including this researcher) ignore this effect.[12] Müller-Krumbhaar *et al.* [60] have overcome this problem by only considering

[12]This problem illustrates one of the two major problems that thwart KMC simulations. The first is where calculating and updating many different rates at each time step becomes too costly and simulations can only be performed over small time scales. A second problem arises if there are many processes occuring with a fast rate that do little to change the state of the system. Here the number of iterations it takes between important events makes the simulation slow. The island growth simulations discussed later are self healing in this regard, that is that the rapid processes of atoms hopping on the surface are gradually frozen out, the mean time step increases, and a new adatom is deposited.

the strain from individual islands locally, and approximating the strains at longer ranges by considering the combined strain from all the islands in each box of a coarse grid.

Numerical simulation of island growth is not conducted exclusively by the KMC method. Ratsch *et al.* [61] have simulated island growth using the "level set method" (LSM). Here the boundaries of each layer of atoms in an island are represented by contours (the level set) in a function which is continuous over the entire substrate. The advantage of this is that the progress of individual atoms is no longer tracked, one instead considers the evolution of a continuous monomer density. The behaviour of the system can be altered in an *ad hoc* manner. In this way Ratsch and coworkers have used the LSM to demonstrate that the distribution of island sizes arises as a result of statistical noise in the nucleation processes (and its sensitivity to the monomer concentration), rather than fluctuations in the growth of islands [55].

3.4.1.3 Scaling

Isotropic island growth exhibits two scaling characteristics. Villain *et al.* [62] proposed that the mean density of stable islands scales with the ratio of flux to the diffusion coefficient, that is

$$\langle n_\chi \rangle \sim \left(\frac{D}{F}\right)^{-\chi}. \tag{3.9}$$

The scaling exponent, χ, is found to vary from $\frac{1}{4}$ to $\frac{1}{2}$. For the case where the critical cluster size, $i = 1$, Evans and Bartelt [54] find that $\chi = \frac{1}{3}$ and $\frac{1}{4}$ for isotropic and infinitely anisotropic (one dimensional) diffusion respectively. Whilst when $i = 2$ they find $\chi = \frac{1}{2}$ and $\frac{1}{3}$. Implicit in these calculations is the idea that the density of stable islands depends on the rate of nucleation of islands alone (islands cannot move). Further it implies that for a given class of growth ($i = 1$, $i = 2$, *etc.*) the nucleation rate evolves with θ in some universal way which scales with the quotient $\left(\frac{D}{F}\right)^{-\chi}$. This scaling form is significant as the island density can be easily measured and so this gives a straightforward way of measuring an isotropic surface diffusion coefficient [63].

A second scaling behaviour is manifest in the distribution of sizes of islands. This scaling exhibits two aspects, the first of these is trivial and arises because there is only one length scale in the problem, namely $\left(\frac{D}{F}\right)^{\frac{1}{4}}$, which acts to set the average island size. The scaling can be clearly understood by realising that the positions of nucleating islands on a surface is *not* completely random. Consider an initially bare substrate upon which an initial

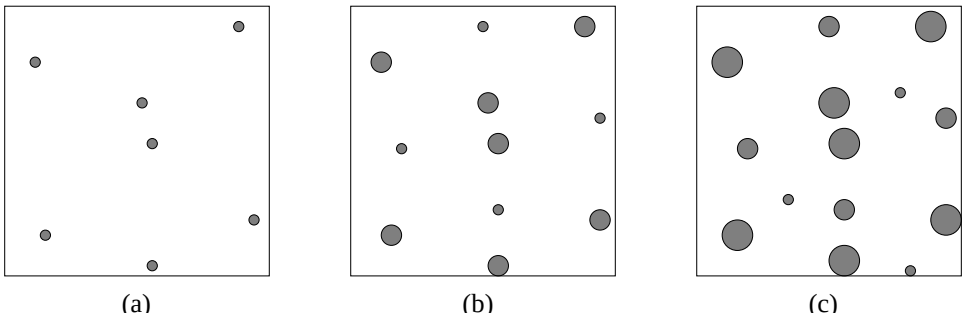

Figure 3.6: Schematic view of the time evolution of adatom islands during the early stages of film growth. Box (a) shows initial random nuclei, (b) and (c) show the time evolution with existing islands growing an the substrate being continually divided into smaller portions as new clusters form in the empty regions between existing islands.

few embryonic clusters form *at random*, this is shown systematically in box (a) of figure 3.6 in which there are empty regions connected by small islands. More atoms are deposited, the later atoms that land near existing islands are more likely to collide with these clusters, while atoms which have a long way to diffuse to existing clusters are more likely to collide with other adatoms and nucleate new clusters. Nucleation is most likely in the middle of the empty regions and so the surface subdivides into smaller empty regions (panel (b) and (c) of figure 3.6). As the process repeats a pattern is created in which the original length scale was set by $\frac{D}{Fb^4}$ (where b is the nearest neighbour atomic distance). Thus micrographs of islands grown to the same overall coverage but with different deposition rates can be made to look the same by simply changing the magnification (providing the average island size is large enough that the size of individual adatoms is negligible). The scale factor required to make micrographs look the same is set by the mean island size.

More formally the average island size is defined to be

$$\bar{s}(\theta) = \sum_{s>1} sP(s,\theta). \tag{3.10}$$

Here $P(s,\theta)$ is defined to be the probability that any atom, picked at random, resides in a cluster of s atoms,

$$P(s,\theta) = \frac{s\langle n_s\rangle}{\sum_{s\geq 2}\langle n_s\rangle}. \tag{3.11}$$

It is observed (in physical and numerical experiments) that the island size distribution obeys

$$P(s,\theta) = \bar{s}^{-1}(\theta) g\left(\frac{s}{\bar{s}(\theta)}\right), \tag{3.12}$$

where $g(z)$ is a universal function that depends on the critical cluster size i. The distribution, $g(z)$, is narrower for larger critical island sizes, because the nucleation probability of a new island becomes more sensitive to the local monomer density [55].

The subdivision of the surface by nucleation does not continue *ad infinitem*. Rather, as the spaces between islands become smaller the incorporation of monomers at island edges becomes more likely than nucleation. A second, more fundamental (and surprising), aspect of the island size distribution is that the scaling form in 3.12 is obeyed for *any* coverage in the precoalescent regime. This means that the shape of the scaling function, $g(z)$, is maintained during growth even though nucleation slows down and islands continue to grow. Here micrographs of a deposition surface at different times *cannot* be made to look similar by changing their magnification as they have different area coverages. The scaling of island archipelagoes grown to the same coverage with differing $\frac{D}{F}$ is trivial, and simply arises from the way islands nucleate. The scaling of the island size distribution at different coverages, on the other hand, is deeper and arises from the way the evolution of nucleation over time is related to the growth of islands over time.[13]

3.4.2 Rate equations for anisotropic diffusion

The self-consistent rate equation description of irreversible two dimensional island growth is now modified to incorporate anisotropic diffusion. The rate equations 3.7 and 3.8 are rewritten in dimensionless form bt defining θ to be the fraction of substrate covered and setting the area of one lattice site to unity gives $F = \frac{d\theta}{dt}$. The product $D\sigma_s$ is replaced by an unknown function of the anisotropic surface diffusion tensor $H_s(\boldsymbol{D})$.

$$\begin{aligned} \frac{d\langle n_1\rangle}{d\theta} &= \left(1 - \sum_{s\geq 1} p_s \langle n_s\rangle\right) \\ &- \left(p_1\langle n_1\rangle + 2\frac{H_1(\boldsymbol{D})}{F}\langle n_1\rangle^2 + \sum_{s\geq 2}\langle n_s\rangle\langle n_1\rangle\frac{H_s(\boldsymbol{D})}{F}\right) \end{aligned} \tag{3.13}$$

$$\begin{aligned} \frac{d\langle n_s\rangle}{d\theta} &= \left(p_{s-1}\langle n_{s-1}\rangle + \langle n_{s-1}\rangle\langle n_1\rangle\frac{H_{s-1}(\boldsymbol{D})}{F}\right) \\ &- \left(p_s\langle n_s\rangle + \langle n_s\rangle\langle n_1\rangle\frac{H_s(\boldsymbol{D})}{F}\right). \end{aligned} \tag{3.14}$$

[13] The origin of this scaling is not well understood.

It is assumed that the kinetics of adatom attachment at island edges are considerably more rapid than the arrival of atoms at the island edges. Following Bales and Chrzan, the rate of monomer capture by an island of size s is found by considering the flux of monomers to an island edge. The distribution of monomers around an island is estimated by solving the diffusion equation,

$$\frac{\partial n_1(\boldsymbol{r},\theta)}{\partial \theta} = \nabla.\frac{\boldsymbol{D}}{F}.\nabla n_1(\boldsymbol{r},\theta) + \mathcal{J} - \mathcal{S}. \tag{3.15}$$

Here the first term is the diffusive change in the local monomer density, and the second term is a distributed source accounting for the continued deposition of monomers from the vapour,

$$\mathcal{J} = 1 - \sum_{s\geq 1} p_s \langle n_s \rangle . \tag{3.16}$$

The final term in the diffusion equation is a sink term to account for the continuous loss of monomers to islands (and other monomers and impinging vapour atoms). This is approximated by calculating the mean effective sink strength off all the islands and distributing it uniformly over the entire substrate,

$$\mathcal{S} = p_1 \langle n_1 \rangle + 2\frac{H_1(\boldsymbol{D})}{F} \langle n_1 \rangle + \sum_{s\geq 2} \langle n_s \rangle \frac{H_s(\boldsymbol{D})}{F} = n_1(\boldsymbol{r},\theta)\xi^{-1/2}. \tag{3.17}$$

This is equivalent to calculating a mean density of sinks of unit strength, which is related to a characteristic sink separation ξ.

If the diffusion tensor, $\boldsymbol{D}$, only contains diagonal terms (which can certainly be accomplished by rotating the coordinate system providing the deformed lattice remains orthorhombic), the diffusive term on the right hand side of Eqn. 3.15 is

$$\nabla.\frac{\boldsymbol{D}}{F}.\nabla n_1(\boldsymbol{r},\theta) = \frac{D_{xx}}{F}\frac{\partial^2 n_1(\boldsymbol{r},\theta)}{\partial x^2} + \frac{D_{yy}}{F}\frac{\partial^2 n_1(\boldsymbol{r},\theta)}{\partial y^2}. \tag{3.18}$$

where D_{xx} and D_{yy} are the diagonal elements of the diffusion tensor. This expression is rewritten in a new coordinate system parameterised by r and ϕ where $x = \sqrt{\frac{Dxx}{D_o}} r\cos(\phi)$, and $y = \sqrt{\frac{Dyy}{D_o}} r\sin(\phi)$, to give[14]

$$\begin{aligned} \nabla.\boldsymbol{D}.\nabla n_1(\boldsymbol{r},\theta) \;=\; & \frac{\partial^2 n_1}{\partial r^2}\left(D_{xx}r_{,x}^2 + D_{yy}r_{,y}^2\right) + \frac{\partial n_1}{\partial r}\left(D_{xx}r_{,x,x} + D_{yy}r_{,y,y}\right) \\ & + 2\frac{\partial n_1}{\partial r\partial \phi}\left(D_{xx}\phi_{,x}r_{,x} + D_{yy}\phi_{,y}r_{,y}\right) + \frac{\partial n_1}{\partial \phi}\left(D_{xx}\phi_{,x,x} + D_{yy}\phi_{,y,y}\right) \\ & + \frac{\partial n_1^2}{\partial \phi^2}\left(D_{xx}\phi_{,x}^2 + D_{yy}\phi_{,y}^2\right). \end{aligned} \tag{3.19}$$

[14] r is a scalar and not the position vector $\boldsymbol{r}$.

Here D_o has the dimensions of a diffusion coefficient $[L^2T^{-1}]$ but is as yet undefined. The terms of the form $\alpha_{,\beta}$ and $\alpha_{,\beta,\gamma}$ are the first and second partial differentials $\frac{\partial\alpha}{\partial\beta}$ and $\frac{\partial^2\alpha}{\partial\beta\partial\gamma}$. The new coordinate system stretches the x and y directions relative to the speed of diffusion in those directions so that the right hand side of Eqn. 3.19 simplifies to the Laplacian in cylindrical coordinates,

$$\nabla.\boldsymbol{D}.\nabla n_1(\boldsymbol{r},\theta) = D_o\left(\frac{\partial^2 n_1}{\partial r^2} + \frac{1}{r}\frac{\partial n_1}{\partial r} + \frac{1}{r^2}\frac{\partial^2 n_1}{\partial \phi^2}\right). \tag{3.20}$$

If D_o is chosen to be $\sqrt{D_{xx}D_{yy}}$ the area of the substrate remains the same in the new coordinate system and the dispersed sink density remains unchanged. This is equivalent to stretching the x axis by a factor λ and the y direction by a factor $\frac{1}{\lambda}$, where $\lambda = \left(\frac{D_{xx}}{D_{yy}}\right)^{\frac{1}{4}}$. The partial differential equation in 3.15 can be reduced to an ordinary differential equation by comparing the rate of change of the local density of monomers with the mean density of monomers,

$$\frac{F}{D_o}\left(\frac{d\langle n_1\rangle}{d\theta} - \frac{\partial n_1}{\partial\theta}\right) = -\left(\frac{\partial^2 n_1}{\partial r^2} + \frac{1}{r}\frac{\partial n_1}{\partial r} + \frac{1}{r^2}\frac{\partial^2 n_1}{\partial\phi^2}\right) + \left(\frac{n_1 - \langle n_1\rangle}{D_o\xi^2}\right) \approx 0. \tag{3.21}$$

The approximation to zero is justified when $\frac{D_o}{F}$ is sufficiently large (compared to the square of the atomic area) so the term on the left hand side can be neglected (the adiabatic approximation). This assumes that the shape of the monomer distribution changes very slowly and only the amplitude of the distribution changes significantly with the mean concentration. This approximation removes the time dependence from the problem and yields the Helmholtz equation,

$$\left(\frac{\partial^2 n_1}{\partial r^2} + \frac{1}{r}\frac{\partial n_1}{\partial r} + \frac{1}{r^2}\frac{\partial^2 n_1}{\partial\phi^2}\right) = \left(\frac{n_1 - \langle n_1\rangle}{D_o\xi^2}\right), \tag{3.22}$$

in which the variables r and ϕ can be separated. The Helmholtz equation can be solved for the boundary conditions that the monomer density reaches the mean field value infinitely far from the island and the monomer density is zero at the island edge. The simplest solution occurs when the perimeter of an island of size s (or its containment area if it is fractal) lies on a constant value of $r = r_s$ in the diffusion weighted cylindrical coordinate system. This implies the islands are elliptical with an aspect ratio of λ^2. This will be the case if perturbations at the island edge can relax with sufficient speed to prevent a growth instability in the island shape but without relaxing so fast that the island becomes circular. A stronger argument can be in which the detailed shape of the island is unimportant provided

that the monomer depletion field around the growing island is roughly elliptical with an aspect ratio λ^2. This will be the case if the island does not exhibit a growth instability (*i.e.*, growing in a needle shape in the direction of slowest diffusion[15]). When the deviation of the island from circular matches the stretching of the coordinate system the angular dependence of the concentration disappears, and the Helmholtz equation reduces to that of Bales and Chrzan. Thus solving for $n_1(r,\theta)$ subject to the conditions that $n_1(r_s,\theta)=0$ and $n_1(r\to\infty,\theta)=\langle n_1(\theta)\rangle$ yields

$$n_1(r,\theta)=\langle n_1(\theta)\rangle\left(1-\frac{K_0(r/\xi)}{K_0(r_s/\xi)}\right), \tag{3.23}$$

Where $K_j(x)$ is a modified Bessel function of order j. The capture coefficients can now be found by equating the rate of monomer capture with the flux perpendicular to the island perimeter,

$$\langle n_1(\theta)\rangle\, H_s(\boldsymbol{D})=\oint_\Gamma \left(\boldsymbol{D}.\nabla n_1(\boldsymbol{\Gamma},\theta)\right).\hat{\boldsymbol{p}}(\boldsymbol{\Gamma})dl(\boldsymbol{\Gamma}), \tag{3.24}$$

where $\boldsymbol{\Gamma}$ is the tracking vector of the perimeter of the island, and $\hat{\boldsymbol{p}}(\boldsymbol{\Gamma})$, and $dl(\boldsymbol{\Gamma})$ are the outward unit vector perpendicular to the island edge, and the elemental perimeter length at $\boldsymbol{\Gamma}$, respectively.[16] Parameterising the edge of the island with the angle ϕ in the stretched cylindrical coordinates gives

$$\hat{\boldsymbol{p}}(\boldsymbol{\Gamma}) = \frac{\{-dy,dx\}}{\sqrt{dx^2+dy^2}}, \tag{3.25}$$

$$dl(\boldsymbol{\Gamma}) = \sqrt{dx^2+dy^2}, \tag{3.26}$$

$$\boldsymbol{D}.\nabla n_1(\boldsymbol{\Gamma},\theta) = \left\{D_{xx}\left(n_{,r}r_{,x}+n_{,\phi}\phi_{,x}\right), D_{yy}\left(n_{,r}r_{,y}+n_{,\phi}\phi_{,y}\right)\right\}. \tag{3.27}$$

Substituting these into 3.24 gives the integral

$$\langle n_1(\theta)\rangle\, H_s(\boldsymbol{D})=\sqrt{D_{xx}D_{yy}}\int_{\phi=0}^{2\pi} r_s\left.\frac{\partial n_1}{\partial r}\right|_{r=r_s} d\phi. \tag{3.28}$$

This leaves the capture coefficient proportional to the geometric mean of the diagonal elements of the diffusion tensor

$$H_s(\boldsymbol{D})=2\pi\sqrt{D_{xx}D_{yy}}\frac{r_s}{\xi}\left(\frac{K_1\left(r/\xi\right)}{K_0\left(r_s/\xi\right)}\right). \tag{3.29}$$

This, at first sight, is not surprising as an island on a substrate with anisotropic diffusion depletes the monomers from the same area of substrate in a given time as an island on an

[15] In this instability there is no depleted region ahead of the island in the extended direction, rather monomers move to the fast moving fronts laterally along the direction of fast diffusion.

[16] This is a vector and must not be confused with the scalar gradient energy coefficient Γ.

isotropic surface with diffusion coefficient $\sqrt{D_{xx}D_{yy}}$. This result predicts that the geometric mean of the diffusion tensor is the *only* important parameter in the evolution of the density of stable islands, $\langle n_\chi \rangle$, with θ. It must be noted that the mean field approximation fails to capture the island size distribution, and thus the treatment outlined above gives no information about whether the universal function $g(s/\bar{s}(\theta))$ in Eqn. 3.12 is lost with anisotropy.

In fact, as is demonstrated in the next section, the result found above is only accurate for relatively small diffusion anisotropies. Moreover, the erroneous predictions of this model at large anisotropies hints at a more general failing of macroscopic diffusion descriptions of island growth.

3.4.3 KMC simulations

A KMC code has been written to simulate two dimensional irreversible island growth on a square lattice. The purpose of this code is to investigate the consequences of the crowdion diffusion mechanism hypothesised above and to see if it exhibits behaviour that can be distinguished from diffusion by simple hopping (or kickout) in a real experiment. For this reason the number of allowed process are kept to the minimum that will give the crowdion diffusion behaviour.

3.4.3.1 Rates and processes

The dynamics are limited to include only six possible hopping processes, the rates of which are defined in a lookup table. The first three processes are accessible to isolated monomers (atoms with no first nearest neighbours). These are are simple hopping in the [110] and [$\bar{1}$10] directions (defined to be the x and y directions respectively with rates R_x and R_y), and the formation of a crowdion (with rate R_c). The movement of a crowdion is assumed to be more rapid than the total rate at which any event occurs on the substrate. Thus the rate of crowdion transport is limited by the rate of crowdion formation alone and the jump (as with all the other permitted processes) is assumed to be instantaneous. Hence there are no crowdion-crowdion interactions. A crowdion is restricted to travelling in the $\pm x$ direction and only along one of the two atomic rows the adatom is initially sitting between (see figure 3.7). A crowdion jumps d_c lattice spacings before ejecting the atom at its centre to one of the two rows of surface sites to either side of it. Should the crowdion encounter

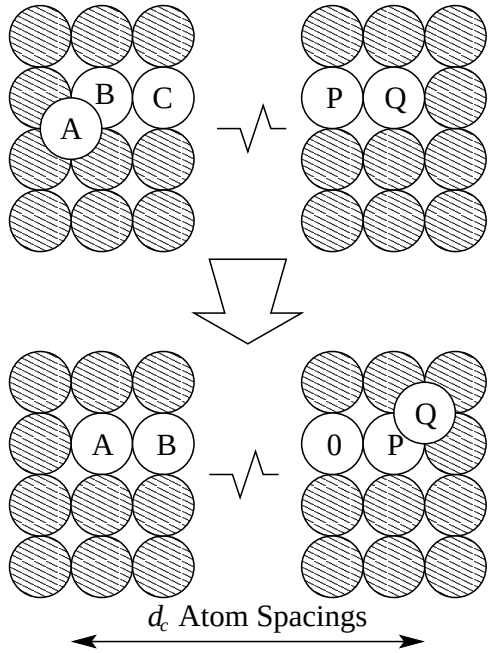

Figure 3.7: Schematic showing the positions of atoms before and after a typical crowdion hop. Unhatched circles represent atoms that move.

any atoms in either of these two rows before travelling d_c the crowdion decomposes, and the ejected atom binds to the surface atom. As calculating the phonon drag of a crowdion is nontrivial d_c is left as a controllable parameter.

There is theoretical evidence to suggest that vacancies in the Cu (001) surface are as mobile as adatoms [64, 65]. As monomers are continually being deposited on the surface during growth is it assumed that the population of monomers is larger that the population of vacancies, thus diffusion by vacancies is ignored.

Two further processes are included in the code that allow islands to move and their shapes to relax. These are hopping along the edge of an island (with rate R_e) and hopping away from a reentrant corner in the island perimeter (with rate R_s), which are shown schematically in figure 3.8. Both of these are independent of the orientation of the island edge, and both include hopping around convex corners in the island edge. In general, atoms with one nearest neighbour can hop clockwise or anticlockwise around an island with rate R_e, atoms with two adjacent nearest neighbours and a next nearest neighbour between them can hop clockwise or anticlockwise with rate R_s, and all other atoms in islands are immobile. The requirement that a step hopping atom have a next nearest neighbour is

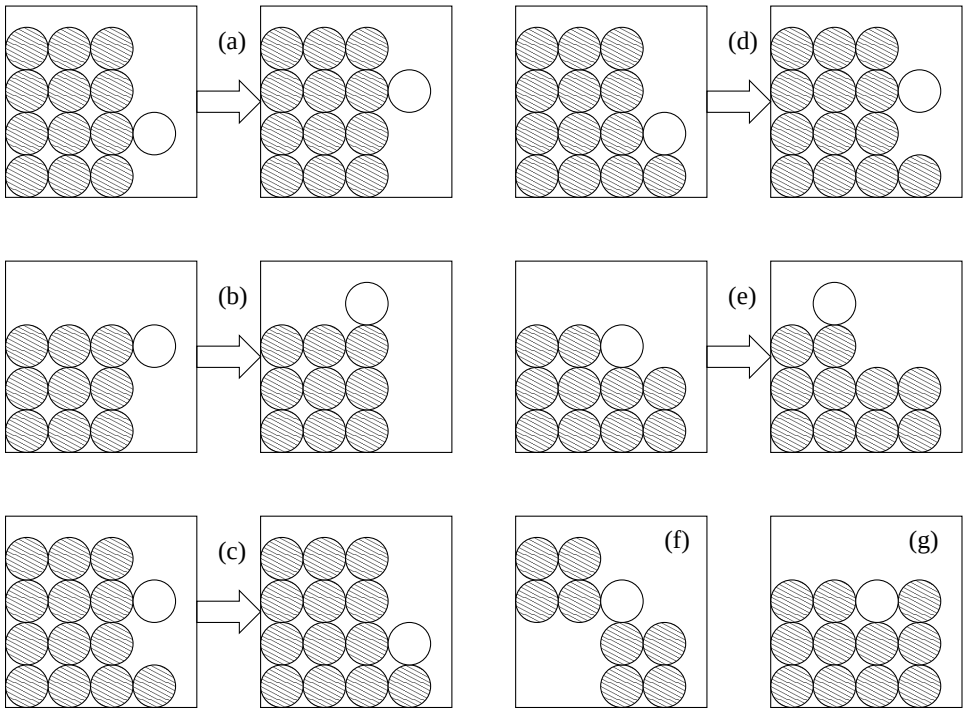

Figure 3.8: Figures showing examples of atom motion at an island edged. The circles represent adatoms on the (001) surface (the substrate atoms are not shown). The mobility of the unhatched atom is considered. Figures (a), (b), and (c) are examples of hopping along an island edge that occurs with rate R_e. Figure (d) and (e) are examples of hopping away from a reentrant step and happen at rate R_s. Panels (f) and (g) show configurations in which the unhatched atom is immobile, in figure (f) the atom must be made immobile in order to not violate detailed balance.

necessary to obey detailed balance. R_s is set to be smaller than R_e, as the hopping atom is initially more highly coordinated for step hopping than edge hopping.

The final ingredient in the KMC code is adatom deposition. Here one site is picked at random to receive a new adatom. Should the picked site lie under an existing island a new site is picked at random from the set of empty sites closest to the original site. This is justified in conditions of two dimensional growth where adatoms that are deposited on top of existing islands diffuse to the island perimeter and are incorporated into the growing island edge.

3.4.3.2 Detailed balance

Detailed balance is the requirement that there be no possible closed sequence of events that changes the total energy of the system. The rates for the three monomer processes are the same everywhere on the bare substrate, and are the same forward and backward, and thus satisfy detailed balance on the substrate as the energy of the system is not changed by the translation of a monomer.

A monomer bonding with another adatom does change the system's energy but forbidding atoms from desorbing from islands removes any closed trajectories of the system which contain this energy change.[17] The mobility of the unshaded atom in configuration (f) figure 3.8 must be zero in order to prevent the desorption of adatoms from islands. It now remains to ensure detailed balance is obeyed by the relaxation processes at the island edge. As both edge hopping and step hopping are independent of the orientation of the island edge, and as both are the same clockwise and anticlockwise detailed balance is obeyed at the island edges and thus the complete model is thermodynamically sound.

[17] This also implies that the energy required to remove an atom from an island edge to the bare substrate is infinite (and this energy must be dissipated over the whole system), just as the energy required to remove a monomer from the otherwise bare substrate to the vapor is infinite. This is a little strange but does not violate the laws of thermodynamics.

3.4.3.3 Diffusion tensor

From these simple island relaxations and equation 3.5 it is trivial to calculate the macroscopic diffusion tensors,

$$\boldsymbol{D}_1 = \frac{b^2}{2} \times \begin{vmatrix} \left(R_x + d_c^2 R_c\right) & 0 \\ 0 & \left(R_y + \frac{R_c}{2}\right) \end{vmatrix}, \tag{3.30}$$

$$\boldsymbol{D}_2 = \frac{b^2 R_e}{4} \times \begin{vmatrix} 1 & 0 \\ 0 & 1 \end{vmatrix}, \tag{3.31}$$

$$\boldsymbol{D}_3 = \frac{5b^2 R_e}{27} \times \begin{vmatrix} 1 & 0 \\ 0 & 1 \end{vmatrix}. \tag{3.32}$$

Here $\boldsymbol{D}_1$, $\boldsymbol{D}_2$, and $\boldsymbol{D}_3$ are the diffusion tensors for monomers, dimers, and trimers respectively, b is lattice parameter of the primitive square surface lattice (*i.e.*, $b = \sqrt{2}a$ where a is the lattice parameter of the FCC lattice), and d_c is the mean squared number of lattice spacings jumped by a crowdion. For the diffusion of trimers one must account for the motion of both "L" shaped trimers and linear trimers. Two of the jump processes of an "L" shaped trimer result in another "L" configuration and two result in a linear configuration, whilst each of the four possible jumps of a linear trimer result in an "L" configuration. Thus on average the population of "L" shaped trimers must be double that of linear trimers. The result in equation 3.32 above averages over the possible trimer configurations weighted by their relative abundance.

Several things are evident from the diffusion tensors above. First, there are an infinite number of combinations of R_x, R_y, R_c and d_c that will give the same monomer diffusion coefficient. Secondly, the rate of diffusion of dimers and trimers only depends on the rate of edge running, R_e. The diffusion of four atom clusters is more complicated; at some point a diffusing tetramer will adopt a square configuration which it can only get out of by an atom jumping away from a reentrant step. If $R_s \ll R_e$ four atom clusters are effectively immobile.[18] In fact if $R_s = 0$ the centre of mass of a growing island can oscillate but the interior of the island will always contain the four atoms that first formed a square (in their original positions).

It would appear that if R_e is sufficiently small in comparison with R_x and R_y then the mobility of dimers and trimers may be neglected and a comparison can be made with

[18] Three is the first "magic number" of a square lattice.

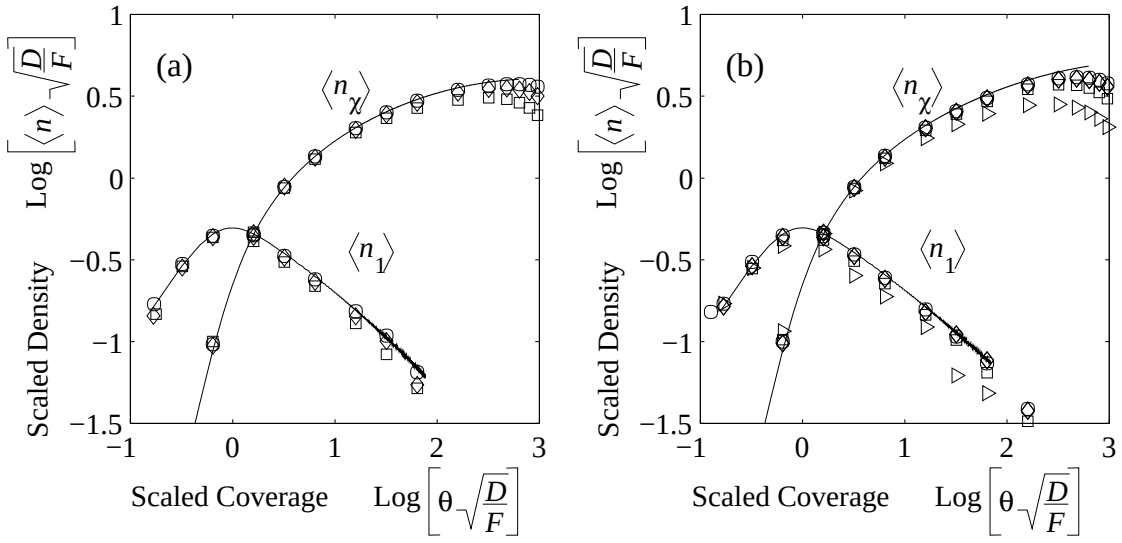

Figure 3.9: Scaled plots of $\langle n_1 \rangle$ and $\langle n_\chi \rangle$ versus θ for fractal (a) and compact(b) islands. In both cases $\frac{\sqrt{D_{xx}D_{yy}}}{F} = 10^7 b^4$, solid lines are calculated from the self-consistent rate equation analysis, and symbols are the results of KMC simulations with anisotropy ratios: $\lambda = 1$ ($\circ$), $\lambda = \sqrt{2}$ ($\diamond$), $\lambda = 2$ ($\square$), and in plot (b) $\lambda = 4$ ($\triangleright$).

the simplest of von Smoluchowski's rate equations. This, however, is not always the case and it is demonstrated below that the distribution of the island sizes, $P(s, \theta)$, is rather sensitive to the rate of edge diffusion for rather simple, but subtle, reasons.

3.4.3.4 Isotropic hopping

Testing The KMC code was tested by comparing the evolution of $\langle n_1 \rangle$ and $\langle n_\chi \rangle$ with θ for isotropic diffusion with the predictions from numerically integrated rate equations. The agreement can be seen in figure 3.9 (circles and the solid lines). Plot (a) shows calculations for fractal islands where no atom mobility is permitted at island edges. Here $p_s \sim s^{2/d_f}$, and $r_s \sim \frac{1}{\sqrt{\pi}} s^{\frac{1}{d_f}}$, where d_f is the fractal dimension. The fractal dimension gives a measure of how the continuous area required to envelope a fractal scales with the area of the fractal itself and can be found by measuring how the "radius of gyration", defined to be r_g, of islands scales with the number of atoms in them. The radius of gyration is defined by [66]

$$r_g = \sqrt{\sum_{i=1}^{s} \frac{\boldsymbol{r}_i^2}{s}}, \tag{3.33}$$

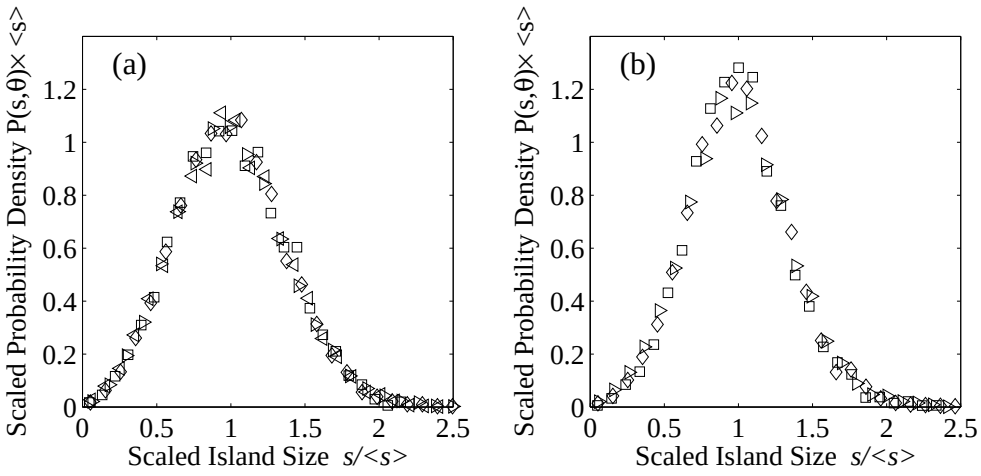

Figure 3.10: Plots of scaled island size distribution ($\bar{s}P(s,\theta)$ vs. $(s/\bar{s})$) under diffusion by isotropic simple hopping. Plot (a) is for fractal islands grown to conditions: $\frac{D}{F} = 10^9 b^4$ and $\theta = 0.2$ ($\Box$), $\frac{D}{F} = 10^8 b^4$ and $\theta = 0.2$ ($\Diamond$), $\frac{D}{F} = 10^7 b^4$ and $\theta = 0.2$ ($\triangleright$), $\frac{D}{F} = 10^7 b^4$ and $\theta = 0.1$ ($\triangleleft$). Plot (b) is for compact islands grown to coverage $\theta = 0.2$ with $R_e = \frac{D}{400 b^2}$, $R_s = \frac{D}{40000 b^2}$, and mobility to flux ratios of: $\frac{D}{F} = 10^9 b^4$ ($\Box$), $\frac{D}{F} = 10^8 b^4$ ($\Diamond$), $\frac{D}{F} = 10^7 b^4$ ($\triangleright$).

where $\boldsymbol{r}_i$ is the displacement vector of the ith atom in the fractal from the fractal's centre (of mass), and the sum is performed over all s atoms in the island. The fractal dimension was calculated from maps of islands at 5 and 10% coverages and found to be 1.7 ± 0.1.

Plot (b) of figure 3.9 show calculations for compact islands where the relaxation of island shapes is included. Here $d_f = 2$, $p_s \sim s$, and $r_s = \alpha\sqrt{s}$, with the fitting parameter $\alpha = 0.95$ for square islands following Bales and Chrzan [2].

All simulations presented here were performed on a 500 atom by 500 atom substrate with periodic boundary conditions. All statistical data from KMC simulations is averaged over 80 simulations.

Island size distribution Figure 3.10 shows scaled plots of $P(s,\theta)$. For fractal islands (plot (a)) the data collapse is excellent for values of $\frac{D}{Fb^4}$ varying over three orders of magnitude, and coverages ranging from 0.1 to 0.2. The same is not true when the islands are compact (plot (b)) where the distributions become narrower and more peaked with increasing $\frac{D}{F}$. This is attributed to the mobility of trimers and dimers that edge running affords.

The origin of the breakdown in scaling is illustrated by figure 3.11 that shows

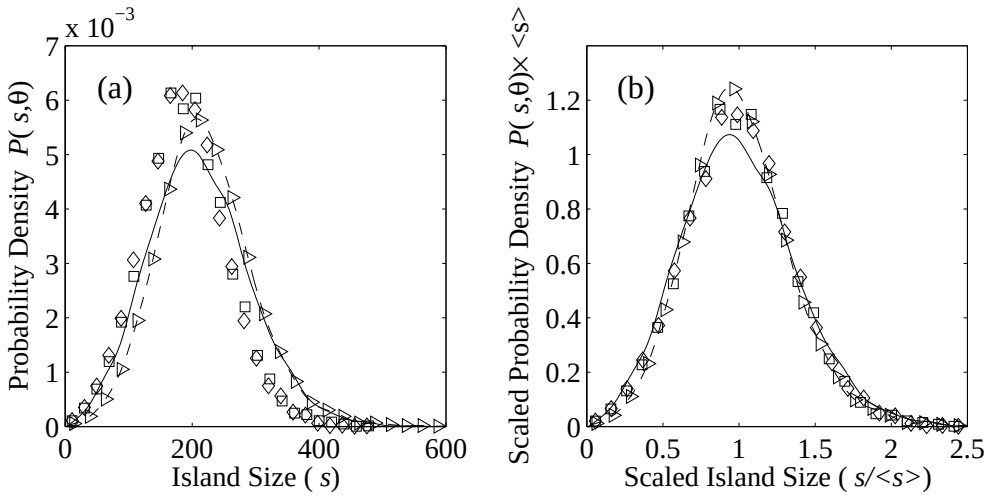

Figure 3.11: Plots of unscaled (a) and scaled (b) island size distribution under diffusion by isotropic simple hopping. Islands were grown to $\theta = 0.2$ under conditions $\frac{D}{F} = 10^7 b^4$ with edge relaxation rates: $R_e = 0$ and $R_s = 0$ ($\circ$), $R_e = \frac{D}{400b^2}$ and $R_s = \frac{D}{40000b^2}$ ($\square$), $R_e = \frac{D}{400b^2}$ and $R_s = 0$ ($\diamond$), $R_e = \frac{D}{40b^2}$ and $R_s = 0$ ($\triangleright$). In plot (b) splines have been fit through the points for the fastest edge relaxation, and no edge relaxation to make the change in shape of the scaling function easier to discern.

unscaled (a) and scaled (b) size distributions of islands grown isotropically with simple hopping and different degrees of edge mobility. Typical archipelago maps for the plots in figure 3.11 are shown in figure 3.12. It can be seen from these figures that as the rate of hopping at island edges increases islands transition from having a fjordal coast line, to being compact and roundish, then compact and facetted. As edge running increases the total density of islands is reduced and the distribution of islands becomes narrower. These results are in agreement with the observations of Ratsch and coworkers [67]. Allowing dimers and trimers to move, albeit slowly, means that some of these clusters are able to diffuse to (and meld with) other existing islands before they have time to be rendered immobile by agglomeration of other monomers. Hence, there is a small but continuous drain on the number of stable clusters nucleated, which acts to reduce both the total number of islands and the fraction of small islands.

Mobility of small clusters has another effect that relates to the nucleation probability. It was stated in section 3.4.1.3 that nucleation is most probable in the regions where the concentration of monomers is largest,[19] similarly a small mobile cluster is most likely

[19]This is an average over time not the area of the substrate.

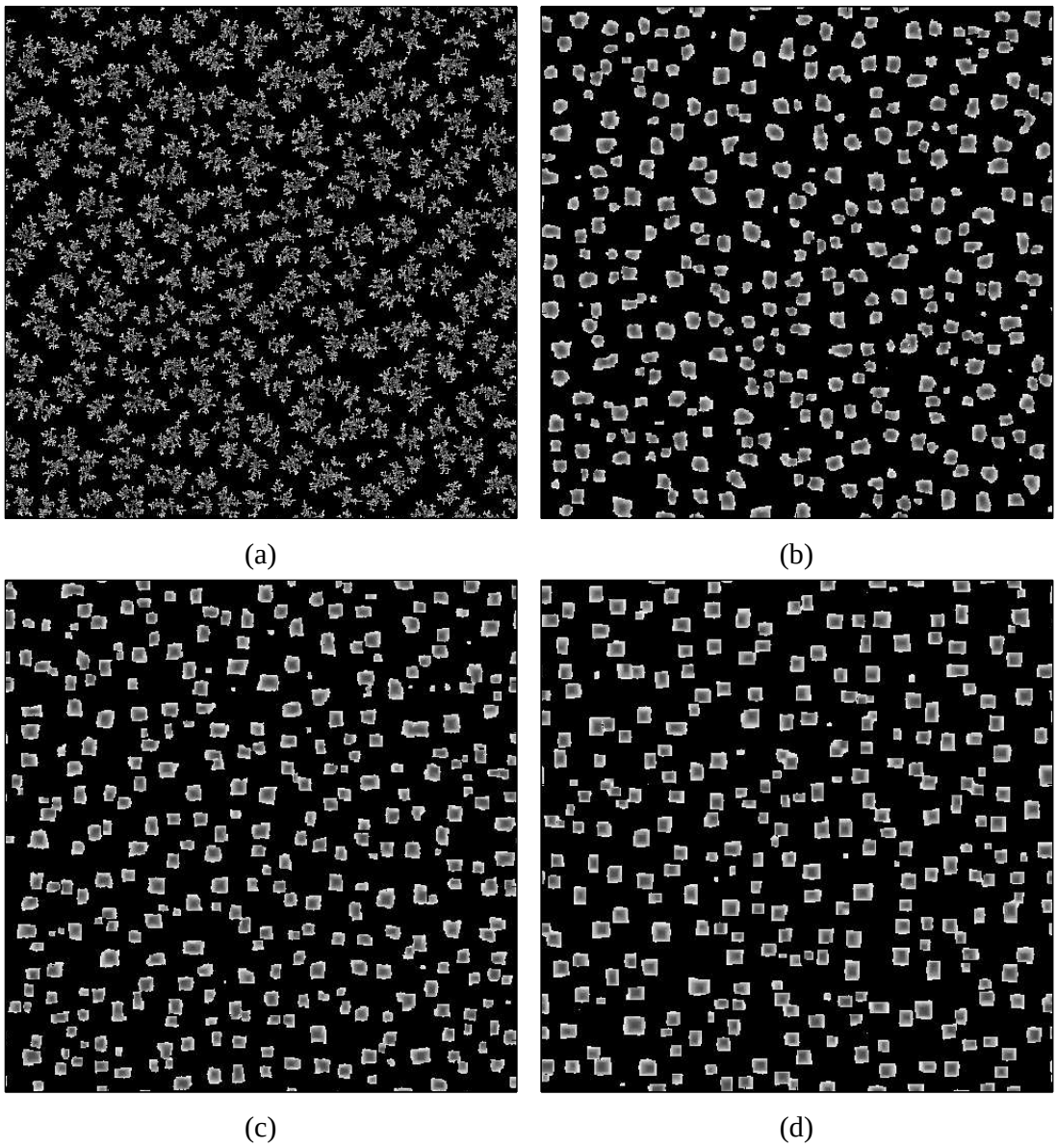

Figure 3.12: Micrographs of island archipelagoes from the KMC simulation. All images are $500b \times 500b$. Black indicates bare substrate while adatoms are shaded from grey to white based on the time they were deposited on the substrate, with white atoms deposited latest. Map (a) shows fractal islands with *no* relaxations at island edges ($R_e = R_s = 0$). Chart (b) shows rounded compact islands for which $R_e = \frac{D}{400b^2}, R_s = 0$. Maps (c) and (d) shows larger square compact islands for which $R_e = \frac{D}{40b^2}, R_s = 0$, respectively

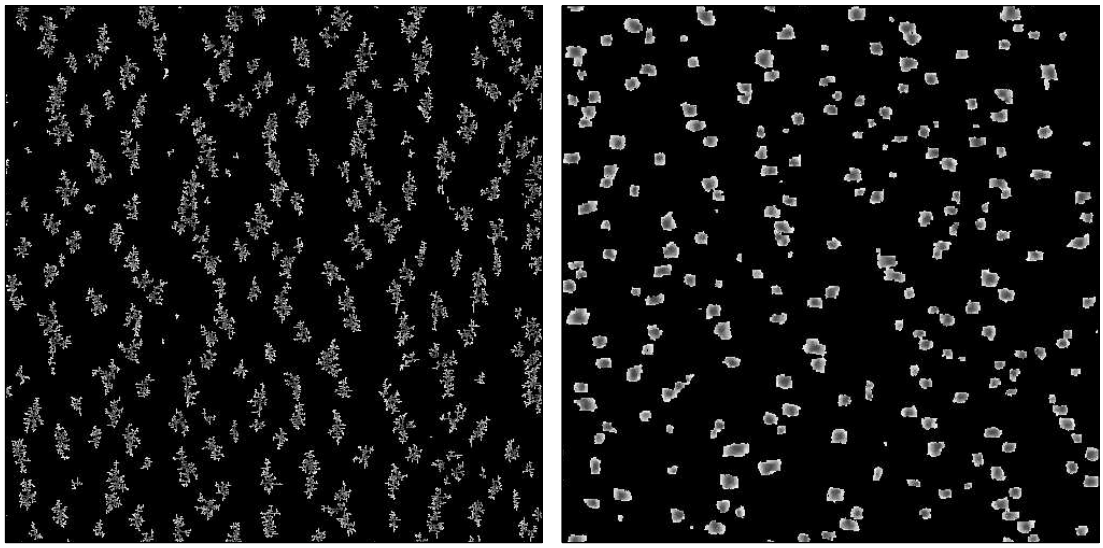

(a) (b)

Figure 3.13: Micrographs of islands at $\theta = 0.1$ grown with $\frac{D_o}{F} = 10^7$ with: $\lambda = 2$ and *no* edge mobility (a), and $\lambda = 4$ with island shapes able to relax (b). Images dimensions are $500b \times 500b$. Diffusion is fastest in the horizontal direction.

to engage another adatom in these regions. Thus, with dimers created near existing islands being "swallowed" by the islands, and dimers distant from island becoming immobile, the effective nucleation of immobile islands is more sensitive to the local concentration of monomers than the nucleation of dimers is (*i.e.*, $n_1(\boldsymbol{r})^2$): the effective critical island size has been increased.

3.4.3.5 Anisotropic hopping

Number density of stable islands The anisotropy of diffusion is characterised by the parameter $\lambda = \left(\frac{D_{xx}}{D_{yy}}\right)^{\frac{1}{4}}$, and the magnitude of the diffusion coefficient is defined by the geometric mean $D_o = \sqrt{D_{xx}D_{yy}}$. Plots of $\langle n_\chi \rangle$ versus θ are shown in (a) and (b) of figure 3.9 for simple hopping with varying degrees of anisotropy. From these plots two things are apparent. First increasing anisotropy reduces the density of stable islands, and second, islands begin to coalesce at lower coverages.

It can be seen from figure 3.9 that the number density of islands decreases more quickly with diffusion anisotropy for the case of fractal islands than compact islands. The cause is evident in the snapshot of the island archipelago for each case (figure 3.13). The

fractal islands show a growth instability. These islands are elongated in the direction of slow diffusion. As there is no mobility of atoms at the island edge a perturbation in the island shape can only heal if the perturbation reduces the outward velocity of the growing island's perimeter. An asperity at the island periphery protruding in the slow direction of diffusion can grow rapidly by depleting the monomers from the regions of substrate laterally (in the fast direction) on either side of it. Thus the islands in map (a) of figure 3.13 extend in the slow direction creating depleted regions along the long edges but with very little depletion ahead of their fast growing tips. Clearly this violates the assumption made in the rate equations analysis in section 3.4.2 that the islands (or at least their depleted regions) have an aspect ratio of λ^2, and so one should not expect fractal islands simulations to agree with the mean field theory.

From chart (b) of figure 3.13 it can be seen that the islands for the shape relaxing calculation remain roughly circular, even with a diffusion anisotropy of $\frac{D_{xx}}{D_{yy}} = 256$, as required by the rate equation analysis. Figure 3.9 shows, however, that even compact islands do not adhere to the mean field predictions (particularly evident in the monomer density for $\lambda = 4$). This indicates that the prediction from section 3.4.2 that the geometric mean of the diffusion tensor is the *only* relevant parameter in the number density of stable islands is flawed.

The systematic deviation in $\langle n_1 \rangle$, and $\langle n_\chi \rangle$ from the isotropic case with increasing λ in figure 3.9 (a) can be understood by considering the number of unique sites visited by a random walker on a square lattice. If the walker steps north, south, east or west with equal probability[20] then the expected number of unique lattice sites that the walker visits, defined to be $\langle N_u \rangle$, after taking N steps asymptotes to [43]

$$\langle N_u \rangle \sim \frac{\pi N}{\ln(N)}, \tag{3.34}$$

and for a one dimensional walk this is

$$\langle N_u \rangle \sim \left(\frac{8N}{\pi} \right)^{\frac{1}{2}}. \tag{3.35}$$

These two cases are the extreme lines in plot (a) of figure 3.14. The random walk on a two dimensional lattice is completely space filling–that is, given an infinite number of steps a walker is certain to return to its starting point.[21] As the walk becomes anisotropic, however,

[20] This is a Plóya walk in two dimensions.

[21] This is not the case for random walks on homogeneous lattices with dimensions larger that two [43].

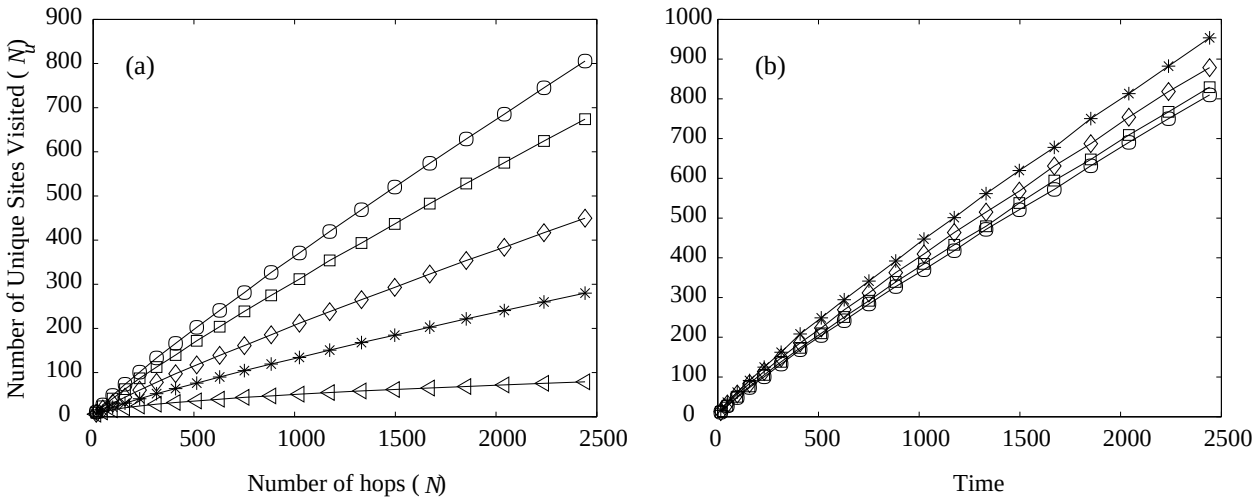

Figure 3.14: Plot of the number of unique sites visited by an isolated random walker hopping N times.

the efficiency with which the random walker searches space is reduced, and the fraction of unique sites visited, $\frac{\langle N_u \rangle}{N}$ diminishes until the extreme case gives one dimensional diffusion.

For diffusion with a constant $\sqrt{D_{xx}D_{yy}}$ however, the number of hops performed in a given time increases with λ ($N \sim D_{xx} + D_{yy}$). The result, as shown in plot (b) of figure 3.14, is that diffusing monomers sample more of the surface lattice in a given time when the diffusion is anisotropic.[22] Clearly this must be important for the early time nucleation of islands when there is only a gas of monomers on the surface. At these times the notion of depleted regions is not applicable and nucleation depends on the time it takes monomers to search an *area* for other monomers, rather than the time it takes a monomer to travel a given *distance* (across a depleted region) to an existing island. The nucleation search area, $\frac{1}{\langle n_1 \rangle}$, decreases as more monomers are deposited on the surface. Thus a slow searching species will nucleate later, and with a higher density of islands, than a fast searching species. This behaviour can clearly be seen in figure 3.9. Once islands have been established and act as sinks for monomers then the distance an adatom has to travel to an island becomes important.

It must be noted that the diffusion coefficient only gives information on the distances that atoms move in a given time, not the area they search. Hence, rate equation

[22] Obviously this enhancement of the search area with diffusion anisotropy is also occurring for fractal islands.

formulations that rely only on macroscopic diffusion (such as that in section 3.4.2 along with that of Bales and Chrzan [2], and Family *et al.* [68]) overlook some of the physics of the problem (and hence the good agreement between these theories and numerical experiments must be, at least to some small extent, fortuitous).

Coalescence The KMC simulations exhibit coalescence at lower and lower coverages as diffusion becomes more anisotropic.[23]

Coalescence of islands on isotropic substrates is delayed because as two neighbouring islands approach each other the depletion regions around them overlap and the accretion of monomers in the overlap region is reduced. This slows the growth velocity of the sections of island perimeter that are heading toward collision. The islands screen each other from the sea of monomers as they approach each other. In the case of anisotropic diffusion the depleted regions are highly anisotropic.[24] Thus, the screening in the slow diffusing direction is greatly reduced and coalescence can occur earlier in this direction. It can be clearly seen that in both micrographs in figure 3.13 that the separation between islands is greater in the direction of fast diffusion (the x direction) than in the slow direction.

Island size distribution The shape and scaling behaviour of the island size distribution with hopping anisotropy is examined in figure 3.15. Panel (a) shows scaled plots of $P(s,\theta)$ for fractal islands at a coverage of $\theta = 5\%$.[25] Panel (b) shows the same plots for compact islands. The distributions in both cases are slightly different due to edge running. Remarkably there are no gross deviations in the scaling functions (discernible from the noise) due to anisotropy.

3.4.3.6 Crowdion diffusion

Adatom trajectory and site visitation The diffusion tensor for the hypothesised crowdion diffusion, 3.30, may be simplified by assuming that R_x is of the order of R_y. Thus defining $R_x \approx R_y \approx R_h$ makes the diffusion tensor the sum of an isotropic hopping diffusion tensor, $\frac{b^2 R_h}{2}\begin{vmatrix} 1 & 0 \\ 0 & 1 \end{vmatrix}$, and a highly anisotropic crowdion tensor, $\frac{b^2 R_c}{4}\begin{vmatrix} 1 & 0 \\ 0 & 2d^2 \end{vmatrix}$. On

[23] It must be remembered that the rate equations do not include any terms to account for coalescence and so do not predict it.

[24] For fractal islands screening in the slow diffusion direction is nonexistent!

[25] This low coverage was chosen so that effects of coalescence are avoided.

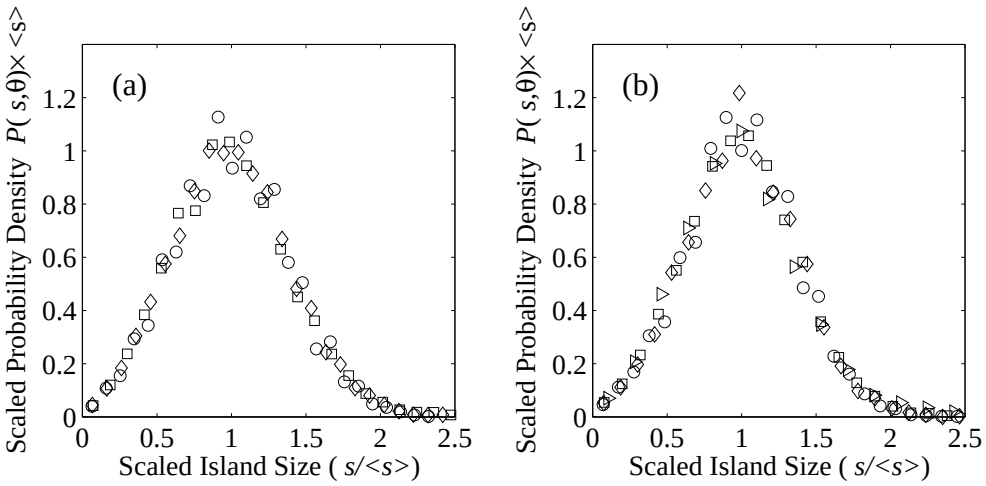

Figure 3.15: Plots of scaled island size distributions at $\theta = 0.05$ grown with $\frac{D_o}{F} = 10^7 b^4$ for fractal (a), and compact (b) islands. Diffusion anisotropies: $\lambda = 1$ ($\circ$),$\lambda = \sqrt{2}$ ($\diamond$),$\lambda = 2$ ($\square$),$\lambda = 4$ ($\triangleright$)(in (b) only).

inspection, one can see two ranges of the diffusion tensor that lead to qualitatively different trajectories of a diffusing adatom (figure 3.16). The first of these has $R_h = O(R_c)$ (trajectory (a) in figure 3.16). In this case crowdions are as likely to occur as simple hops. The trajectory looks like that of an anisotropically hopping random walker; there are large regions of the surface which have a high density of site visitation. In the other extreme the rate of crowdion formation can be very small in comparison to the hop rate ($R_h \ll R_c$), this is shown by trajectory (b) of figure 3.16. Trajectory (a) is qualitatively different than path (b), which has relatively few crowdion jumps but the jumps are large enough to carry the walker well away from the area it has already searched. Between these big jumps are local areas which are heavily explored by isotropic hopping.

The path of the adatom diffusing with large crowdion jumps looks *similar* to the trajectory of a Lévy walk (in one dimension).[26] Lévy walks are a class of random walks in which the second moment of the jump probability distribution is infinite.[27] These walks have no intrinsic length scale, the trajectory is self-similar.[28] This is not the case for the

[26]Strictly speaking this is a Lévy flight as each jump is assumed to happen instantaneously

[27]To have an infinite second moment of the jump length probability distribution means that the distribution must decay algebraically. It should be noted that this implies that species diffusing by a Lévy walk will have an *infinite* diffusion coefficient as infrequent long jumps cannot be neglected (in the same way that the elastic interaction between dislocations separated by large distances cannot be neglected). The diffusion length of a Lévy walk scales linearly with time.

[28]A simple hopping walk is also self-similar in the sense that there is no length scale to the fluctuations

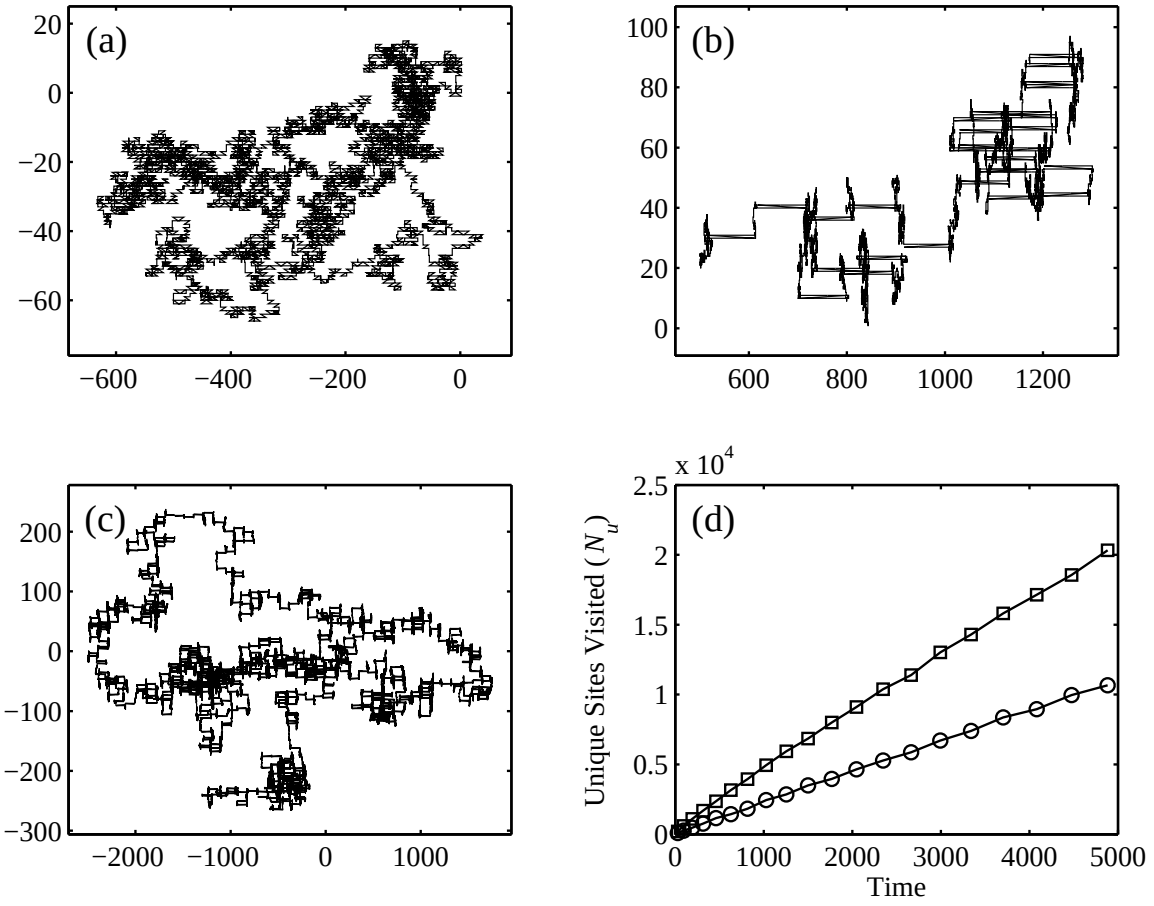

Figure 3.16: Panels (a), (b), and (c) show trajectories of diffusing adatoms moving by crowdion jumping and simple hopping. In all cases the diffusion tensors are identical with $\sqrt{D_{xx}D_{yy}} = \frac{1}{2}$ (atomic units squared per time unit) and $\lambda = \left(\frac{D_{xx}}{D_{yy}}\right)^{\frac{1}{4}} = 2\sqrt{2}$ and hopping is isotropic. In panel (a) the diffusion jump length, d_c, is 10 atomic spacings, whilst in (b) and (c) it is 100. The trajectories in (a) and (b) are 4000 time units long, whilst (c) is 80000. It can be seen that the diffusion trajectories in (a) and (b) are qualitatively different, while increasing the increasing the diffusion time of the (b) to (c) yields a trajectory that resembles (a). It must be noted that the scales of the x and y axes are different in plots (a), (b) and (c) and in all cases the numbers given are atomic spacings. Plot (d) shows the number of unique sites visited with time for the two sets of diffusion parameters. The squares are for diffusion with $d_c = 10$, and the circles are for $d_c = 100$.

crowdion walk (whose jump probability distribution is Gaussian and does have a finite second moment); increase the diffusion time and the perambulation resembles ordinary hopping again. This can be seen from trajectory (c) in figure 3.16. The implications of this are that if the qualitatively different trajectory impacts island growth then the time scale over which atoms diffuse is also important, and there will be a window of growth parameters where island growth behaves differently (if it is going to). Bychuk and O'Shaughnessy [69] observe anomalous diffusion of adatoms on a solid liquid interface where Lévy type diffusion arises (over a limited time scale) because adatoms can appear to make large jumps by desorbing from the surface and diffusing through the liquid before reabsorbing to the surface. Amar, Family and Hughes [59] perform KMC simulations for growth of fractal islands in the presence of true Lévy diffusion where the probability of a jump of length Δx is given by $P(\Delta x) \sim \Delta x^{-d_s-\beta_L}$, where d_s is the dimensionality of the substrate, and β_L is the Lévy exponent that determines the length of the tails of the probability distribution. Normal diffusive ($\sqrt{Dt}$) behaviour occurs for $\beta_L \geq 2$, whilst $2 > \beta_L \geq 1$ is referred to as "enhanced diffusion", and $\beta_L \leq 1$ is "ballistic" diffusion. These researchers find that the island density scaling exponent, χ, for both one and two dimensional diffusion rises with decreasing Lévy exponent.

Stable island density Two sets of KMC simulations that included crowdion hopping were performed. In both cases the simple surface hopping was set to be isotropic. In one case the mean squared crowdion jump length d_c was 10 atom spacings and in the other it was 50 atom spacings. Figure 3.17 shows the evolution of the density of stable islands with coverage for anisotropic diffusion with different extents of crowdion jumping. There are two features in these plots worthy of comment. First, the number density of islands and monomers rises sharply with increasing d_c. This is consistent with the reduction in the area searched by the crowdion flight as the jump length is increased.[29] Numerical calculations of the area searched as a function of time (in scaled units) are shown in figure 3.18.

A second, more interesting observation, is the delayed coalescence of fractal islands due to the increasing the crowdion jump length. The origin of this behaviour lies in the shape of the island: the embedding area of fractal islands grown with larger values of d_c becomes more circular, and thus coalescence in the slow diffusing direction is delayed.

in the displacement, rather than no intrinsic jump length as is the case for Lévy walks.

[29] As $d_c \to \infty$ the isotropic hopping diffusion tensor $D_h \to \frac{D_s}{\lambda^2}$, and the increased area searched with each crowdion jump only scales linearly with d_c.

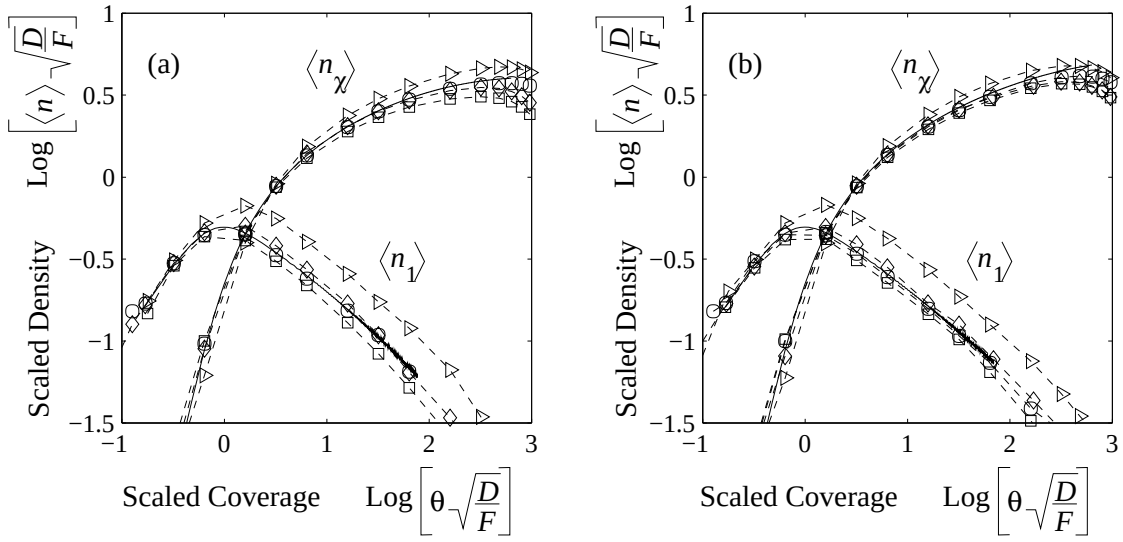

Figure 3.17: Plots of $\langle n_\chi \rangle$ and $\langle n_1 \rangle$ vs θ for islands grown with crowdion diffusion and mobility to flux ratio $\frac{D_o}{F} = 10^7 b^4$. Plot (a) is calculated for fractal islands and plot (b) for compact islands. In both plots solid lines are the result of mean field calculations and symbols (and dashed lines) are the results of KMC simulations for: $\lambda = 1$ and hopping only ($\circ$), $\lambda = 2$ and hopping only ($\square$), $\lambda = 2$ and crowdions with $d_c = 10$ ($\diamond$), and $\lambda = 2$ and crowdions with $d_c = 50$ ($\triangleright$).

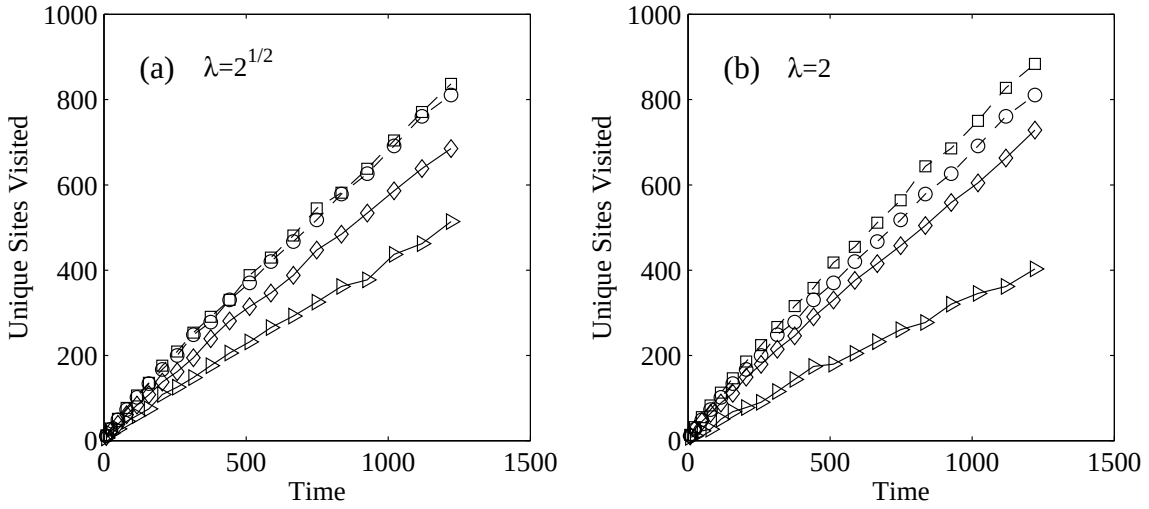

Figure 3.18: Site visitation of random walkers moving by simple hopping (dashed lines) and by crowdion jumping with isotropic hopping with diffusion coefficient $D_o = 1\ b^2 \text{s}^{-1}$. Plot (a) is for $\lambda = \sqrt{2}$, and plot (b) for $\lambda = 2$. Both plots show site visitation for: isotropic hopping ($\circ$), anisotropic hopping ($\square$), and crowdion jumping with $d_c = 10$ ($\diamond$), and $d_c = 50$ ($\triangleright$).

Island-island correlations Figures 3.19 and 3.20 show typical archipelago maps for growth of fractal and compact islands respectively. These figures also show the average island-island correlation functions from 80 simulations, of which each map is an example. The island-island correlation function gives the probability distribution of finding a second island at a position $\boldsymbol{r}$ from island's centre. It is calculated by taking the autocorrelation function of the islands' centres of mass. It can be clearly seen that islands grown with anisotropic hopping exhibit a shape instability, whilst those grown with isotropic short hopping and anisotropic large jumps do not. So crowdions suppress the shape instability. More striking is the denuded (dark) regions in the island-island correlation plots. It can be seen that anisotropic arms of the denuded regions are reduced (in intensity but not in length) when the crowdion jump length increases. This means that the screening by islands becomes more isotropic with increasing d_c. Both of these observations can be explained by more closely examining the diffusion in the neighbourhood of the island edge. This will be done by considering macroscopic diffusion where the concentration gradients are ensemble averages.

Fick's first law, and the definition of the diffusion coefficient, are appropriate only in regions with a slowly varying concentration gradient (relative to the jump length).[30] At the island edge the concentration gradient changes abruptly, so within d_c lattice spacings of the island the simple diffusive model is no longer appropriate.

The transport of monomers to an island edge can be broken into two regions: an outer region greater than d_c from the island edge where diffusion is fast and crowdions can be included in Fick's first law, and an inner region in which half of the crowdion formation events instantly remove monomers to the island edge (the other half move atoms to the outer region). The inner region can be modeled by slow isotropic diffusion with a distributed sink strength given by the crowdion formation rate. This can be seen in concentration profiles from numerical simulations of diffusion to a sink edge in figure 3.21. Thus, the island edge sees an *isotropic* slow diffusion field. So, providing perturbations in island size do not poke through the inner isotropic region the asperities gain no extra growth velocity and the island shape is stable.

[30]It can be seen by working through the simple derivation of Fick's first law for diffusion with atomic jumps of l lattice spacings that one must assume the gradient in concentration is uniform over $2l$ lattice spacings.

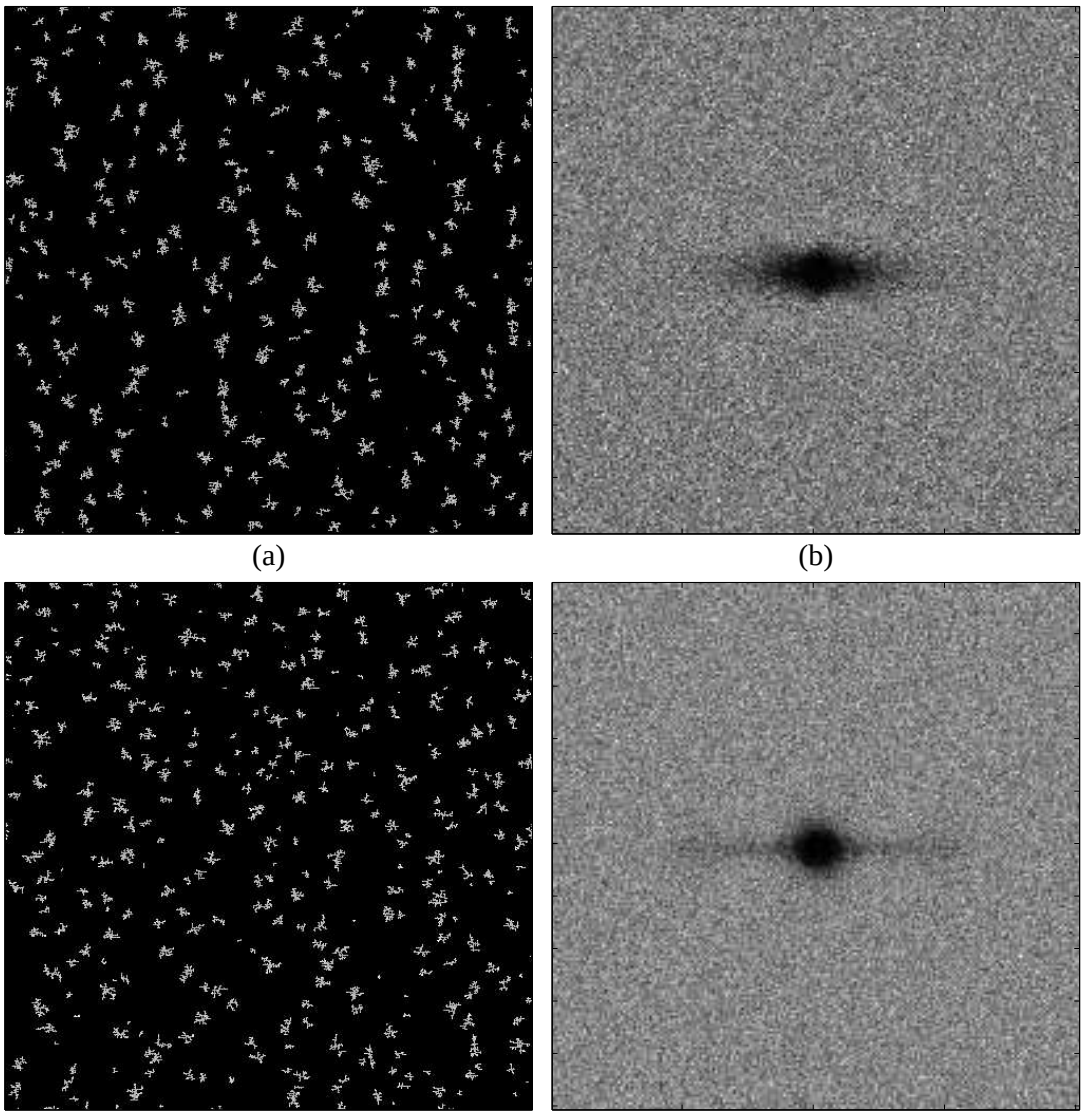

(a) (b)

(c) (d)

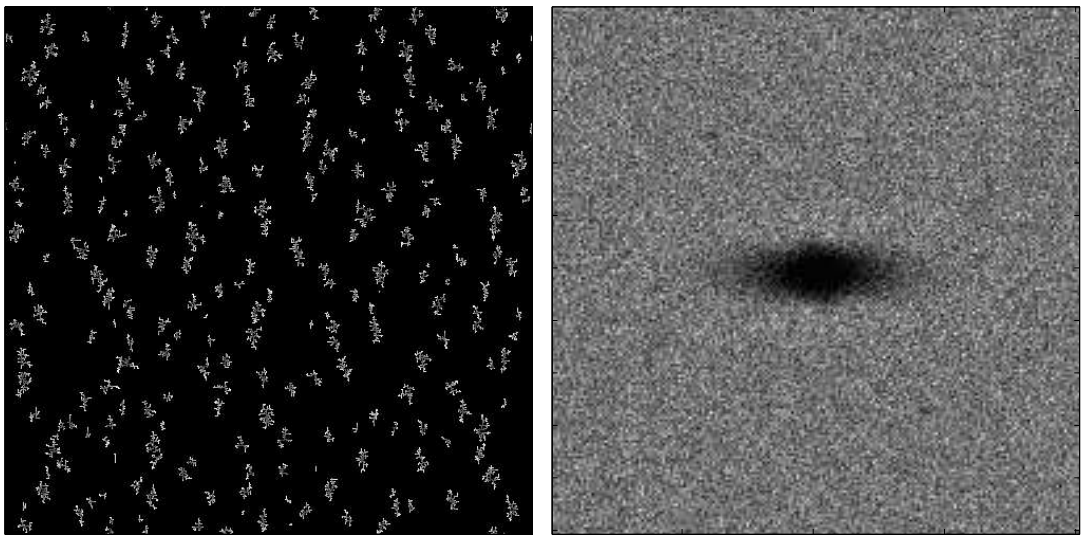

(e) (f)

Figure 3.19: Micrographs of islands and corresponding island-island correlations plots (averaged over 80 maps) at coverage $\theta = 0.05$, grown under fractal growth conditions with $\frac{D_o}{F} = 10^7 b^4$ and $\lambda = 2$. Plots (a) and (b) (on the previous page) have isotropic hopping and crowdion jump length $d_c = 10$, (c) and (d) have isotropic hopping and crowdion jump length $d_c = 50$, and (e) and (f) have anisotropic hopping with no crowdions. The islands in (a) and (c) have been shaded uniformly white, as the majority of the atoms in the islands are atoms that were originally in the substrate. Maps are $500b \times 500b$, whilst island-island correlations are $200b \times 200b$. Dark regions in the island-island correlations represent areas with few inter-island vectors.

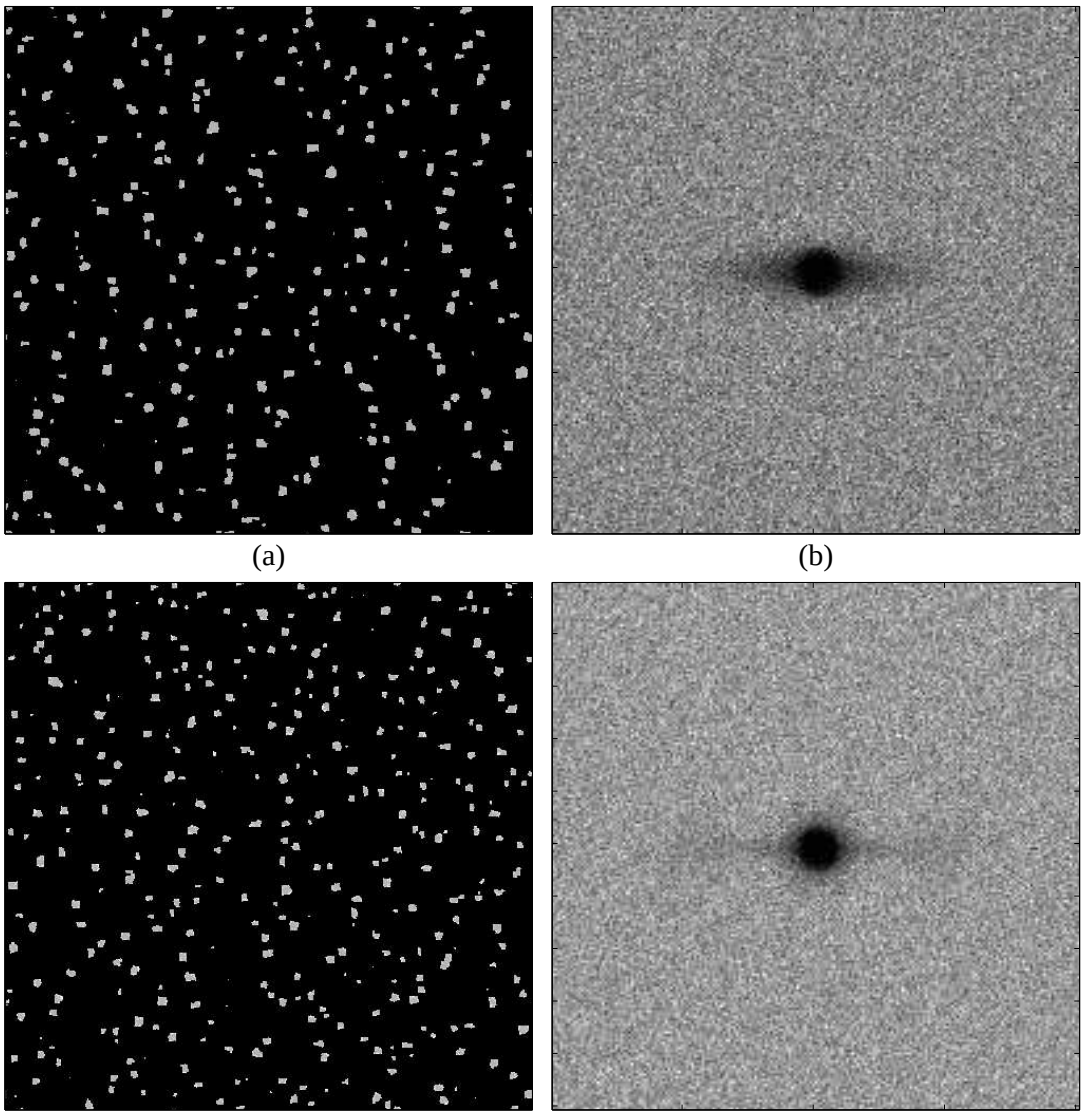

(a) (b)

(c) (d)

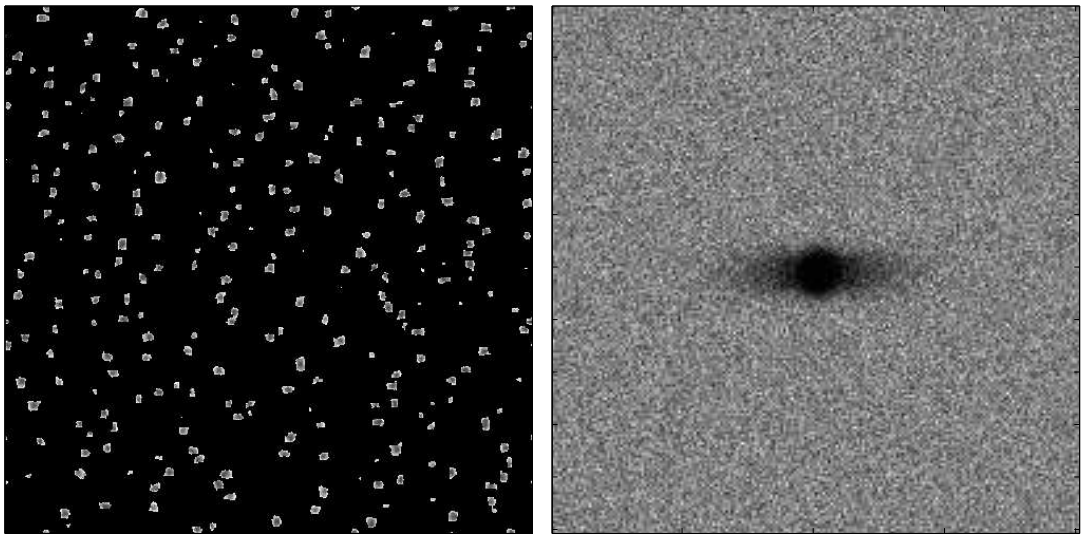

(e) (f)

Figure 3.20: Micrographs of islands and corresponding island-island correlations plots (averaged over 80 maps) at coverage $\theta = 0.05$, for compact islands grown with $\frac{D_o}{F} = 10^7 b^4$ and $\lambda = 2$. Plots (a) and (b) (on the previous page) have isotropic hopping and crowdion jump length $d_c = 10$, (c) and (d) have isotropic hopping and crowdion jump length $d_c = 50$, and (e) and (f) have anisotropic hopping with no crowdions. The islands in (a) and (c) have been shaded uniformly white, as the majority of the atoms in the islands are atoms that were originally in the substrate. Maps are $500b \times 500b$, whilst island-island correlations are $200b \times 200b$.

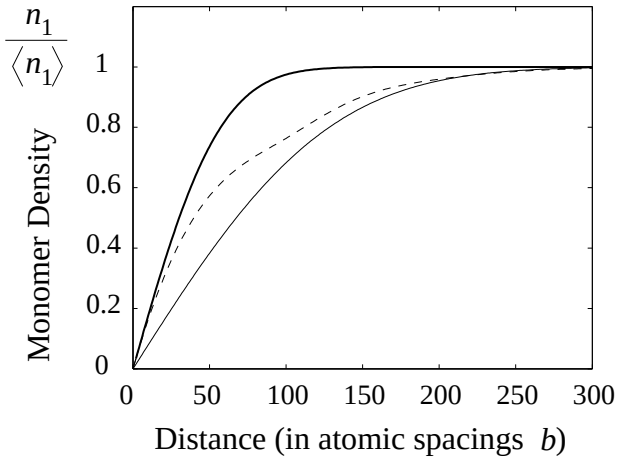

Figure 3.21: Concentration profiles near an island edge calculated numerically after 10^5 time units. Thin solid line is calculated for nearest neighbour hopping with a $R_h = 1$, the dashed line is for hopping and crowdion diffusion with the same diffusion coefficent as before and $R_h = 0.2$, $R_c = 8 \times 10^-5$, and jump length $d_c = 100$, and the thick solid line is calculated for simple hopping only with hopping rate $R_h = 0.2$.

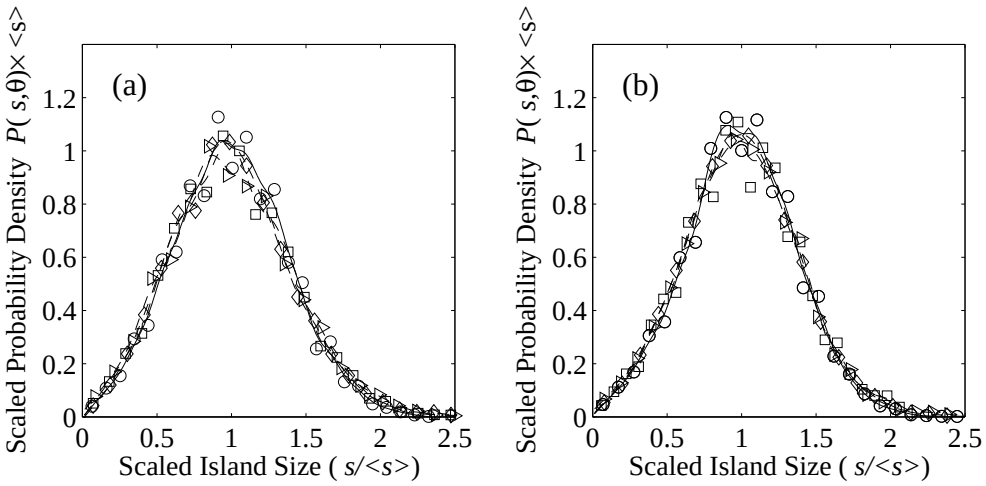

Figure 3.22: Plots of scaled island size distributions at $\theta = 0.05$ grown with $\frac{D_o}{F} = 10^7 b^4$ for fractal (a), and compact (b) islands. Mobility parameters: $\lambda = 1$ with hopping only ($\circ$), $\lambda = 2$ with hopping only ($\diamond$), $\lambda = 2$ with isotropic hopping and crowdions with jump length $d_c = 10$ ($\square$), $\lambda = 4$ with isotropic hopping and crowdions with jump length $d_c = 50$ ($\triangleright$).

Island size distribution The mode of diffusion seems to have little impact on the shape if the island size distribution. Figure 3.22 show the size distributions for fractal and compact islands, and although both of these distributions have a slightly different shape, they are changed little by the transport mechanism (smoothing splines have been fit through the data).

3.4.3.7 Scaling exponent χ

The scaling exponent χ (in equation 3.9) is calculated by finding the gradient of a least squares straight line fit to the plot of $\log_{10}(\langle n_\chi \rangle)$ versus $\log_{10}\left(\frac{D_o}{F}\right)$ (shown in figure 3.23). The exponent is found to increase for both crowdions and fractal islands from $\chi = 0.33$ for isotropic hopping to $\chi = 0.34$, $\chi = 0.35$ and $\chi = 0.36$ for anisotropic diffusion (with $\lambda = 2$) for; no crowdions, and crowdions with jump lengths $d_c = 10$, and $d_c = 50$, respectively. This could indicate that over the length and time scales associated with an adatom moving to an island the transport *appears* to exhibit "enhanced" diffusion. Amar *et al.* [59] see χ rise from 0.24 to 0.29 for one dimensional diffusion, and go from 0.34 to 0.38 for two dimensional diffusion as β_L is diminished from 4.0 to 1.33 (and the tails of the jump probability distribution become wider). The situation for crowdion diffusion is

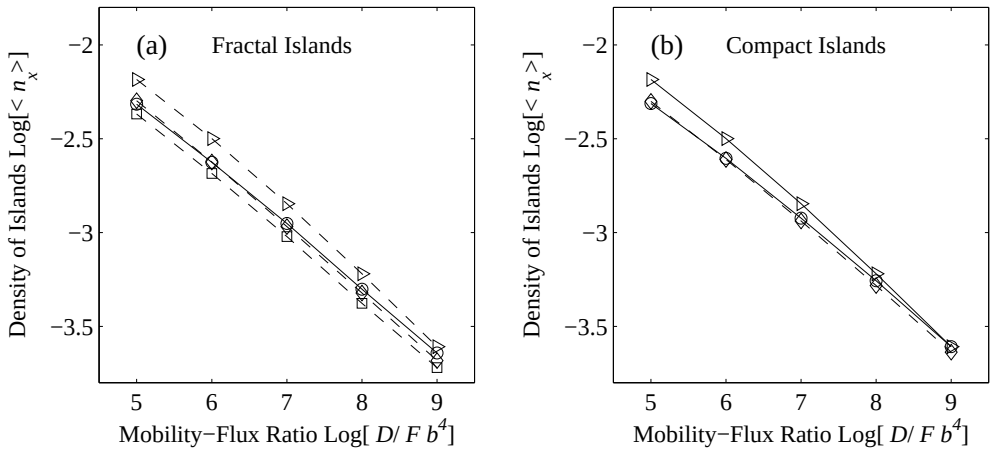

Figure 3.23: Plot of $\langle n_\chi \rangle$ vs. $\frac{D_o}{F}$ for fractal (a) and compact (b) islands grown with: isotropic hopping ($\circ$ and solid line), $\lambda = 2$ with anisotropic hopping only ($\Box$), $\lambda = 2$ with isotropic hopping and a crowdion jump distance $d_c = 10$ ($\Box$), $\lambda = 2$ with isotropic hopping and a crowdion jump distance $d_c = 50$ ($\triangleright$).

somewhat more complicated as here one dimensional "enhanced" diffusion is embedded in a two dimensional diffusion field.

Ratsch *et al.* [67] see an increase in the scaling exponent from 0.33 to 0.38 with increasing edge mobility from $\frac{R_e}{R_h} = 0.001$ to $\frac{R_e}{R_h} = 0.1$ as the effective critical island size rises above unity. As the site searching ability of the crowdion is reduced with increasing d_c, small clusters have more time to diffuse between collisions with monomers, which increases their relative mobility. It is possible that this accounts for the increasing χ for compact islands but does not acount for the change in χ for fractal islands where there is *no* edge running.

Linderoth *et al.*, [49] and Günther *et al.* [70] have measured the χ for island growth on the quasihexagonal reconstruction of Pt(001) and Au(001), respectively. These researchers measure scaling exponents that are at odds with predictions from their thorough KMC investigations. As it is demonstrated above that diffusion with long jumps affects the scaling exponent it is possible that the values of χ measured for these "hex" reconstructed surfaces arise due to some long range self-diffusion mechanism, a possibility overlooked by both sets of researchers. This is warrants further investigation.

Detecting crowdion growth It was demonstrated above that there is an observable difference between island growth in the presence of the postulated crowdion diffusing mech-

anism, and the islands grown by anisotropic simple hopping with the same diffusion tensor. While distinguishing crowdion behaviour by comparison of simulations is straightforward, experiment offers no such comparison.[31]

The scaling exponent, χ, is one experimental observable impacted by crowdions, but edge running or other anomalous diffusion processes must be ruled out, and experiments must determine χ very accurately. Similarly, the shape of fractal islands is another observable by which crowdions might reveal themselves. However, one must observe islands with circular embedding areas in the presence of strongly anisotropic diffusion. This would require seeing long denuded arms in the island-island correlations (these can be weak but must be long). This however requires temperatures low enough to freeze out edge diffusion (so that the islands are fractal) but not so low that crowdions are also frozen out.

3.5 Conclusions

In this last chapter a new long-range adatom *self*-diffusion mechanism was described, and some routes to experimentally observing it were outlined. The influence of these crowdions on island growth was compared to anisotropic nearest neighbour hopping. A continuum rate equation description of submonolayer island growth has been extended to include anisotropic hopping diffusion. It was found that continuum treatments of island growth are poor for systems with highly anisotropic diffusion. This is because macrosopic diffusion theories assume that mass transport behaves macroscopically the same independent of the transport mechanism. While this is certainly the case over large scales, this is not true over small scales such as near island edges or in small area searching (for monomers *etc.*).

It was demonstrated that crowdions do give rise to qualitatively different island growth behaviour but there is no obvious signature that can determine their presence in a real growth experiment.

Finally, it was suggested that a metastable displacive long ranged diffusion mechanism, similar in spirit to that postulated for a crowdion, may be in operation on the "hex" reconstructed (001) surfaces of FCC metals. As such, data for island growth on these surfaces should be reexamined with this in mind.

[31] There is only the experimental data there is no data from a known diffusion type with which to compare.

Bibliography

[1] Dieter Weller and Andreas Moser. Thermal effect limits in ultrahigh density magnetic recording. *Transactions on Magnetics*, 35(6):4423–39, November 1999.

[2] G. S. Bales and D. C. Chrzan. Dynamics of irreversible island growth during submonolayer epitaxy. *Physical Review B*, 50(9):6057–68, September 1994.

[3] J. C. P. Chang, T. P. Chin, and J. M. Woodall. Incoherent interface of InAs grown directly on GaP(100). *Applied Physics Letters*, 69(7):961, August 1996.

[4] F. K. LeGoues, J. Tersoff, M. C. Reuter, M. Hammar, and R. M. Tromp. Relaxation mechanism of Ge islands/Si(001) at low temperature. *Applied Physics Letters*, 67(16):2317–9, October 1995.

[5] A. E. Romanov, P. M. Petroff, and J. S. Speck. Lateral ordering of quantum dots by periodic subsurface stressors. *Applied Physics Letters*, 74(16):2280–2, April 1999.

[6] M. I. Larsson, R. F. Sabiryanov, K. Cho, and B. M. Clemens. Surface strain effects on adatom kinetics and self-assembly. *Surface Science Letters*, 536(1-3):L389–95, June 2003.

[7] R. F. Sabiryanov, M. I. Larsson, K. Cho, W. D. Nix, and B. M. Clemens. Surface diffusion and growth of patterned nanostructures on strained surfaces. *Physical Review B*, 67(12):125412–19, March 2003.

[8] M. I. Larsson, R. F. Sabiryanov, K. Cho, and B. M. Clemens. Nanopatterning of periodically strained surfaces: Predictive kinetic monte carlo simulation study. *Journal of Applied Physics*, 94(5):3470–84, September 2003.

[9] Harald Brune, Marcella Giovannini, Karsten Bromann, and Klaus Kern. Self-organized growth of nanostructure arrays on strain-relief patterns. *Nature*, 394(6692):451–3, July 1998.

[10] John W. Cahn and John E. Hilliard. Free energy of a nonuniform system. III. nucleation in a two-component incompressible fluid. *The Journal of Chemical Physics*, 31(3):688–99, September 1959.

[11] John W. Cahn. On spinodal decomposition. *Acta Metallurgica*, 9(8):795–801, September 1961.

[12] John W. Cahn. Phase separation by spinodal decomposition in isotropic systems. *The Journal of Chemical Physics*, 42(1):93–99, January 1965.

[13] Frank Glas. Elastic state and thermodynamical properties of inhomogeneous epitaxial layers: Application to immiscible III-V alloys. *Journal of Applied Physics*, 62(8):3201–8, October 1987.

[14] I. P. Ipatova, V. G. Malyshkin, and V. A. Shchukin. On spinodal decomposition in elastically isotropic epitaxial films of III-V semiconductor alloys. *Journal of Applied Physics*, 74(12):7198–210, December 1993.

[15] R. J. Asaro and W. A. Tiller. Interface morphology development during stress-corrosion cracking. I. via surface diffusion. *Metallurgical Transactions*, 3(7):1789, July 1972.

[16] D. J. Srolovitz. On the stability of surface of stressed solids. *Acta Metallurgica*, 37(2):621–5, February 1989.

[17] Frank Glas. Thermodynamics of a stressed alloy with a free surface: Coupling between the morphological and compositional instabilities. *Physical Review B*, 55(17):11277–86, May 1997.

[18] Frank Glas. Thermodynamic and kinetic instabilities of lattice-matched alloy layers: Compositional and morphological perturbations. *Physical Review B*, 62(11):7393–401, September 2000.

[19] F. Jonsdottir and L. B. Freund. Equilibrium surface roughness of a strained epitaxial film due to surface diffusion induces by interface misfit dislocations. *Mechanics of Materials*, 20(4):337–49, June 1995.

[20] J. E. Guyer and P. W. Voorhees. Morphological stability of alloy thin films. *Physical Review B*, 54(16):11710–24, October 1996.

[21] J. E. Guyer and P. W. Voorhees. Morphological stability of alloy thin films. *Physical Review Letters*, 74(20):4031–4, May 1995.

[22] B. J. Spencer, P. W. Voorhees, and J. Tersoff. Enhanced instability of strained alloy films due to compositional stresses. *Physical Review Letters*, 84(11):2449–52, March 2000.

[23] I. P. Ipatova, V. G. Malyshkin, A. A. Maradudin, V. A. Shchukin, and R. F. Wallis. Kinetic instability of semiconductor alloy growth. *Physical Review B*, 57(20):12968–93, May 1998.

[24] F. Léonard and R. C. Desai. Elastic effects and phase segregation during the growth of thin film alloy layers by molecular-beam epitaxy. *Physical Review B*, 56(8):4955–65, August 1997.

[25] F. Léonard and R. C. Desai. Alloy decomposition and surface instabilities in thin films. *Physical Review B*, 57(8):4805–15, February 1998.

[26] F. Léonard and R. C. Desai. Spinodal decomposition and dislocation lines in thin films and bulk materials. *Physical Review B*, 58(13):8277–88, October 1998. These authors consider dislocation influenced decomposition during the deposition process mediated only by surface diffusion, rather than treating decomposition after deposition.

[27] F. Léonard and R. C. Desai. Atomic ordering and the surface morphology of thin films. *Applied Physics Letters*, 73(2):208–10, July 1998.

[28] J. P. Hirth and J. Lothe. *Theory of Dislocations*. Krieger Publishing Company, Malabar, Florida, second edition, 1992.

[29] A. G. Khachaturyan. *Theory of Structural Transformations in Solids*. Wiley, 1983.

[30] Hanoch Mehl, Ofer Biham, Itay Furman, and Majid Karimi. Models for adatom diffusion on fcc (001) metal surfaces. *Physical Review B*, 60(3):2106–16, July 1999.

[31] Graeme Henkelman and Hannes Jónsson. A dimer method for finding saddle points on high dimensional potential surface using only first derivatives. *Journal of Chemical Physics*, 111(15):7010–22, October 1999.

[32] Peter J. Feibelman. Diffusion path for an Al adatom on Al(001). *Physical Review Letters*, 65(6):729, August 1990.

[33] Ghyslain Boisver and Laurent J. Lewis. Self-diffusion of adatoms, dimers, and vacancies on Cu(100). *Physical Review B*, 56(12):7643–55, September 1997.

[34] Wei Xiao, P. Alex Greaney, and D. C. Chrzan. Adatom transport on strained Cu(001): Surface crowdions. *Physical Review Letters*, 90(15):156102, April 2003.

[35] G. L. Kellog. Field ion microscope studies of exchange-mediated, atom-displacement processes on metal surfaces. *Applied Surface Science*, 87/88:353–63, March 1995.

[36] J. A. Sprague, F. Montalenti, B. P. Uberuaga, J. D. Kress, and A. F. Voter. Simulation of growth of Cu on Ag(001) at experimental deposition rates. *Physical Review B*, 66(20):205415, November 2002.

[37] A. Seeger. Diffusion and thermal conversion of crowdions. *Physica Status Solidi A*, 38(1):235–44, July 1970.

[38] W. Frank, M. Ruhle, R. Schindler, and A. Seeger. Interpretation of electron microscope investigations on ion-bombarded copper, nickle and gold in terms of the crowdion model. *Communications on Physics*, 1(5):125–9, July 1976.

[39] D. I. Pushkarov. Quantum theory of crowdions at low temperatures. *Soviet Physics JETP*, 37:322, 1973.

[40] N. H. March and D. I. Pushkarov. Mass transport by crowdions: a simple model appropriate to body-centred-cubic Na and K. *Journal of Physics and Chemistry of Solids*, 57(1):139–40, February 1995.

[41] Wei Xiao. Unpublished research.

[42] P. H. Dederichs and K. Schroeder. Anisotropic diffusion in stress fields. *Physical Review B*, 17(6):2524–35, March 1978.

[43] Barry D. Hughes. *Random Walks and Random Environments*, volume Volume 1: Random Walks. Oxford University Press, 1995.

[44] X.-C. Guo, A. Hopkinson, J. M. Bradley, and D. A. King. Corrugation of the reconstructed Pt100 surface: a helium diffraction study. *Surface Science*, 278(3):263–9, November 1992.

[45] K. H. Rieder, T. Engle, and R. H. Swendsen. A helium diffraction study of the reconstructed Au(100) surface. *Surface Science*, 127(2):223–42, April 1983.

[46] M. A. van Hove, R. J. Koestner, P. C. Stair, J. P. Bibérian, L. L. Kesmodel, I. Bartoš, and G. A. Somorjai. The surface reconstructions of the (100) crystal faces of iridium, platinum and gold. *Surface Science*, 103(1):189–217, February 1981.

[47] F. Ercolessi, M. Parrinello, and E. Tosatti. Au (100) reconstruction in the glue model. *Surface Science*, 177(2):314–28, December 1986.

[48] J. J. Mortensen, T. R. Linderoth, K. W. Jacobsen, E. Lægsgaard, I. Stensgaard, and F Besenbacher. Effects of anisotropy diffusion and finite island size in homoepitaxial growth Pt on Pt (100)-hex. *Surface Science*, 400(1-3):290–313, March 1998.

[49] T. R. Linderoth, J. J. Mortensen, K. W. Jacobsen, E. Lægsgaard, I. Stensgaard, and F Besenbacher. Homoepitaxial growth of Pt on Pt (100)-hex: effects of strongly anisotropic diffusion and finite island sizes. *Physical Review Letters*, 77(1):87–90, July 1996.

[50] Y. Miyazawa, J. Lothe, J.-Y. Parlange, and G. M. Pound. Mayer's theory of condensation and homogeneous nucleation. *Journal of Applied Physics*, 42(1):476, January 1971.

[51] M. von Smoluchowski. Three discourses on diffusion, brownian movement and the coagulation of colloidal particles. *Physikalische Zeitschrift*, 17:557–71, and 585–99, November and December 1916.

[52] J. A. Venables. Nucleation and growth of thin films. *Reports on Progress in Physics*, 47(4):399–459, April 1984.

[53] J. A. Venables. Rate equation approaches to thin film nucleation kinetics. *Philosophical Magazine*, 27(5):697–738, May 1973.

[54] J. W. Evans and M. C. Bartelt. Nucleation and growth in metal-on-metal homoepitaxy: Rate equations simulations and experiments. *Journal Vacuum Science and Technology*, 12(4):1800–8, July/August 1994.

[55] C. Ratsch, M. F. Gyure, S. Chee, M. Kang, and D. D. Vvedensky. Fluctuations in scaling and aggregation phenomena. *Physical Review B*, 61(16):R10598–601, April 2000.

[56] Mihail N. Popescu, Jacques G. Amar, and Fereydoon Family. Rate equation approach to island size distribution and capture numbers in submonolayer irreversible growth. *Physical Review B*, 64(20):205404–17, November 2002.

[57] Jacques G. Amar, Mihail N. Popescu, and Fereydoon Family. Self-consistent rate approach to irreversible submonolayer growth in on dimension. *Surface Science*, 491(1-2):239–54, September 2001.

[58] Fereydoon Family, Mihail N. Popescu, and Jacques G. Amar. Self-consistent rate equation theory of cluster size distribution in aggregation phenomena. *Physica A*, 306(1-4):129–39, April 2002.

[59] Jacques G. Amar, Fereydoon Family, and David C. Hughes. Submonolayer epitaxial growth with long-range (Lévy) diffusion. *Physical Review E*, 58(6):7130–6, December 1998.

[60] F. Gütheim, H. Müller-Krumbhaar, and E. Brener. Epitaxial growth with elastic interaction: Submonolayer island formation. *Physical Review E*, 63(4):41603–6, October 2001.

[61] C. Ratsch, M. F. Gyure, R. E. Caflisc, F. Gibou, M. Kang, J Garcia, and D. D. Vvedensky. Level-set method for dynamics in epitaxial growth. *Physical Review B*, 65(19):195403–15, May 2002.

[62] J. Villain, A. Pimpinelli, and D. E. Wolf. Layer by layer growth in molecular beam epitaxy. *Comments on Condensed Materials Physics*, 16(1):1, 1992.

[63] Y. W. Mo, J. Kleiner, M. B. Webb, and M. G. Lagally. Activation energy for surface diffusion of Si on Si(001): A scanning-tunnelling-microscopy study. *Physical Review Letters*, 66(15):1998–2001, April 1991.

[64] Majid Karimi, Tom Tomkowski, Gianfranco Vidali, and Ofer Biham. Diffusion of Cu on Cu surfaces. *Physical Review B*, 52(7):5364–74, August 1995.

[65] Ulrike Kürpick and Talat S. Rahman. Monovacancy diffusion on Ag(100), Cu(100), and Ni(100): Prefactors and activation barriers. *Physical Review B*, 59(16):11014–9, April 1999.

[66] Tamás Vicsek. *Fractal Growth Phenomena*. World Scientific, 1989.

[67] C. Ratsch, M. C. Wheeler, and M. F. Gyure. Roughening due to edge diffusion for irreversible aggregation. *Physical Review B*, 62(19):12636–9, April 2000.

[68] Jacques G. Amar and Fereydoon Family. Critical cluster size: island morphology and size distribution in submonolayer epitaxial growth. *Physical Review Letters*, 74(11):2066–9, March 1995.

[69] Oleg V. Bychuk and Ben O'Shaughnessy. Anomalous diffusion at liquid surfaces. *Physical Review Letters*, 74(10):1795–8, March 1995.

[70] S. Günther, E. Kopatzki, M. C. Bartelt, J. W. Evans, and R. J. Behm. Anisotropy in nucleation and growth of two-dimensional islands during homoepitaxy on "hex " reconstructed Au(100). *Physical Review Letters*, 73(4):553–6, July 1994.